RESEARCH ARTICLE

Editor's Choice

ADVANCED MATERIALS INTERFACES Open Access

www.advmatinterfaces.de

Solvent-Free Phase Separation of Polystyrene-*block*-poly(2-hydroxyethyl methacrylate) Forming Freestanding Photonic Films

Martina Plank, Enis Musa Saritas, Bart-Jan Niebuur, Tobias Meckel, Dirk Lellinger, Peter Krolla, Markus Biesalski, Tobias Kraus, and Markus Gallei**

A solvent-free approach to the formation of freestanding photonic material from amphiphilic polystyrene-*block*-poly(2-hydroxyethyl methacrylate) (PS-*b*-PHEMA) is reported, where the application of shear force and pressure induces phase separation. This work demonstrates access to high molecular weight (HMW; >100 kg mol^{-1}) PS-*b*-PHEMA with PHEMA contents up to 62 vol% using sequential anionic polymerization. By exploring hot pressing, the dependency of microstructure formation on temperature, pressure, and time is demonstrated using transmission electron microscopy and small-angle X-ray scattering measurements. Within 30 min, phase-separated block copolymer (BCP) films are obtained. Although no highly ordered equilibrium structures are formed, photonic properties are observed for PS-*b*-PHEMA films with molecular weights higher than 140 kg mol^{-1} and PHEMA contents between 20 and 51 vol%. The photonic properties are investigated by ultraviolet–visible (UV–vis) and fluorescence spectroscopy as well as confocal fluorescence microscopy. The BCP films exhibit tailored transmittance that is dependent on molecular weight and microstructure, making them suitable for UV and blue light filter applications. Also, structure-dependent reflection and fluorescence are demonstrated. Finally, the application in the field of sensors is addressed by demonstrating a reversible color change of BCP films with a co-continuous microstructure, achieved through polar solvent infiltration and evaporation.

1. Introduction

Nanostructured materials based on block copolymers (BCPs) gained enormous attention in the last decade due to the accessibility of tailored functional materials with tunable properties using the bottom-up process with high precision even on a sub-20 nm scale.[1,2] Thus, BCPs have found their way into applied sciences, such as energy storage,[3] photonic materials,[4,5] membrane technology,[6,7] and many more, helping to push the boundaries in material science and tackle global challenges.[8]

Of particular interest are BCPs with a high Flory–Huggins interaction parameter χ, which are essential to obtain sub-10 nm structures and enable access to microstructures with domain sizes larger than 100 nm.[9,10] The χ parameter indicates the degree of segregation of the various covalently connected block segments of a BCP. Thus, BCPs such as polystyrene-*b*-poly(4-vinylpyridine)

M. Plank, E. M. Saritas, T. Meckel, M. Biesalski
Ernst-Berl Institute of Technical and Macromolecular Chemistry
Technische Universität Darmstadt
64287 Darmstadt, Germany
E-mail: martina.plank@kit.edu

M. Plank, P. Krolla
Institute of Functional Interfaces (IFG)
Karlsruhe Institute of Technology (KIT)
76344 Eggenstein-Leopoldshafen, Germany

E. M. Saritas, T. Meckel, M. Biesalski
Institute for Macromolecular and Paper Chemistry
Technical University of Darmstadt
64287 Darmstadt, Germany

B.-J. Niebuur, T. Kraus
INM-Leibniz-Institute for New Materials
Saarland University
66123 Saarbrücken, Germany

D. Lellinger
Division Plastics
Fraunhofer Institute for Structural Durability and System Reliability LBF
64289 Darmstadt, Germany

T. Kraus
Colloid and Interface Chemistry
Saarland University
66123 Saarbrücken, Germany

M. Gallei
Chair in Polymer Chemistry
Saarland University
66123 Saarbrücken, Germany
E-mail: markus.gallei@uni-saarland.de

M. Gallei
Saarene
Saarland Center for Energy Materials and Sustainability
66123 Saarbrücken, Germany

The ORCID identification number(s) for the author(s) of this article can be found under https://doi.org/10.1002/admi.202500593

© 2025 The Author(s). Advanced Materials Interfaces published by Wiley-VCH GmbH. This is an open access article under the terms of the Creative Commons Attribution License, which permits use, distribution and reproduction in any medium, provided the original work is properly cited.

DOI: 10.1002/admi.202500593

21967350, 2026, 1, Downloaded from https://advanced.onlinelibrary.wiley.com/doi/10.1002/admi.202500593 by Saarlandische Universitäts- Und Landesbibliothek Sulb, Wiley Online Library on [03/02/2026]. See the Terms and Conditions (https://onlinelibrary.wiley.com/terms-and-conditions) on Wiley Online Library for rules of use; OA articles are governed by the applicable Creative Commons License

(PS-*b*-P4VP) with a high χ value (χ = 0.30–0.40) exceed the order-disorder transition (ODT) at significantly lower molecular weights than the well-known polystyrene-*b*-poly(methyl methacrylate) PS-*b*-PMMA (χ = 0.021–0.035) and begin to self-assemble.[10] The resulting equilibrium microstructure is determined by the degree of polymerization (N), the block volume fraction (f_i), and χ.[11–13] In general, five different stable microstructures were identified nowadays via field-theoretic simulations (FTSs), including the classical lamellar (L), cylindrical (C), and spherical phase, and two complex network structures referred to as gyroid (G) and *Fddd* (O^{70}).[14]

Recent research has increasingly focused on BCP-derived highly ordered 1D to 3D nanostructures, that exhibit interesting optoelectronic properties, from structural color[4] to complete bandgap formation.[15] Furthermore, chiral and negative refractive index metamaterials have been realized.[5,16–19] At this point, we want to acknowledge the increasing simulation work, which has led to tremendous progress in many scientific fields.[20–23] The fundamentals of the interaction of BCPs with light, as an electromagnetic wave, have already been excellently summarized in recent reviews, to which we refer.[4,5,24–26] Furthermore, Vignolini and co-workers provided an overview of photonic materials derived from BCPs of the past two decades, dividing linear BCPs and brush BCPs applied in multilayer films or colloidal BCP architecture, highlighting PS-*b*-P2VP, ultrahigh molecular weight (UHMW, > 10^3 kg mol^{-1}) BCPs (PS-*b*-PI, PS-*b*-PSM), and ROMP brush polymers as commonly used BCPs.[4,27] In the future, increasing variety will be observed due to significant advances in BCP synthesis,[25,28] as well as enhanced interdisciplinary and simulation work.[14,17,29] In general, photonic materials consist of dielectric building blocks, which can control light propagation due to their structural arrangement. The main principles are multilayer interference,[4] grating diffraction,[30] and bandgap modulation.[19,31] As the polarization of dielectric materials is dependent on their environment, many photonic materials are responsive to stimuli such as temperature, pH value, solvent, mechanical force, electric and magnetic fields as well as to additives (ions and other molecules), which makes them attractive for sensor or bioassay technologies.[24,31]

Since structural colors with stimuli-responsive behavior are easy to realize, e.g., by BCPs forming Bragg mirrors,[4,32] by perfectly ordered colloidal systems,[33–35] or by colloidal glasses exhibiting Mie resonance,[36] the focus of the current research is more on the applicability for the industry. Nowadays, BCP-based metamaterials attract more attention because light can be modulated in completely new ways by customized electromagnetic fields in the final material.[5] Here, research of the last decade shows high potential for complex BCP-derived structures like gyroid, diamond, or other highly periodic three-dimensional structures.[3,15,18,26,37–39] With increased access to a variety of new BCPs and the ability to predict and control the structure, the production of various co-continuous structures is no longer an obstacle.[19,40,41] At the same time, complete bandgap formation was realized by disordered hyperuniform structures, which describe the regime between random and periodic structures capable of efficiently forming a low dielectric contrast bandgap.[42–45] Jain et al. also addressed the "inverse" method in material design using the advances in simulation methods and computing resources.[46] Here, they showed that disordered structures could also outperform perfectly ordered structures in material properties and that the desired design could be easily realized with inverse strategies. Thus, the disordered hyperuniform concept can already be found in BCP research,[26,29,44,47] which is generally aimed more at industrial applicability, as the formation of highly ordered BCP structures is often a complex and time-consuming process.

Nowadays, the fabrication of photonic material based on BCPs might be easy to realize, nevertheless, it goes along with long process times, using methods like solvent, vapor, and temperature annealing as well as magnetic and electrical field alignment over multiple hours and days, which at the same time were restricted to solvent based thin film approaches using harmful solvents like chloroform, dimethylformamide (DMF), acetone, or tetrahydrofuran (THF).[31,48] The reason for this is the entanglement of long polymer chains. The mobility of polystyrene (PS) is already influenced at low molecular weights, such as 31 kg mol^{-1}, which reaches the critical molecular weight M_c, approximately double to triple that of the molecular weight of the entanglement M_e.[49,50] Beyond M_c, the power law for viscosity η ($\eta \propto M^{3.0-3.7}$) depends on the polymer species, which reaches for a very high molecular weight the reptation molecular weight M_r ($M_{r,PS} \approx 430$ kg mol^{-1}), a rubber-like plateau where viscosity gets independent of molecular weight.[49–51] Also, Semenov, who investigated the microphase separation of BCP melts in the strong segregation limit (SSL) confirmed that the relaxation of a melt into most stable states (bcc, fcc, and hcp) needs to be very slow and therefore the thermodynamically favored structure may be inaccessible.[52] Since the last decade, brush BCPs have revolutionized the research field of photonic BCPs, pioneered by the work of Grubbs and co-workers. With the ROMP approach, a wide range of brush BCPs can be realized, exhibiting superior viscoelastic properties that lead to rapid self-assembly.[53–58] Nevertheless, the synthetic strategy is limited by the use of expensive metathesis catalysts, which contain rare metal centers. However, these could be avoided in the future due to a new generation of catalysts or monomer design. Furthermore, the advantages of reversible deactivation radical polymerization (RDRP) should not be disregarded.[27,59,60] All in all, each technology has its *raison d'être* and is better suited to one area of application than another.

In our previous work, high molecular weight (HMW) PS-*b*-PHEMA (>100 kg mol^{-1}) showed a limitation of phase separation in solution-based films with subsequent temperature annealing.[61] This was overcome by introducing a small amount of cellulose (2.9 wt%), which acted like a seed crystal for the microstructure in the vicinity of the cellulose fiber, which reached up to 10 µm in length from the interface.[61] In general, it was shown that cellulose also accelerates the phase separation of PS-*b*-PHEMA with lower molecular weight (<70 kg mol^{-1}), and the temperature annealing step can be shortened from 7 to 2 d to generate comparable long-range order to BCP microstructures with the standard procedure (**Figure 1A**). Nevertheless, greater long-range orderings can be achieved if the process is carried out using cellulose with a 7-d annealing period (Figure 1B). As pre-orientation to extended chains is limited for HMW BCP due to entanglement and reduced solubility of the BCP in THF, solvent-based process is no longer beneficial. Hence, an additional force was needed to be introduced to trigger the phase separation besides using additives. Inspired by the melt-shear process

© 2025 The Author(s). Advanced Materials Interfaces published by Wiley-VCH GmbH

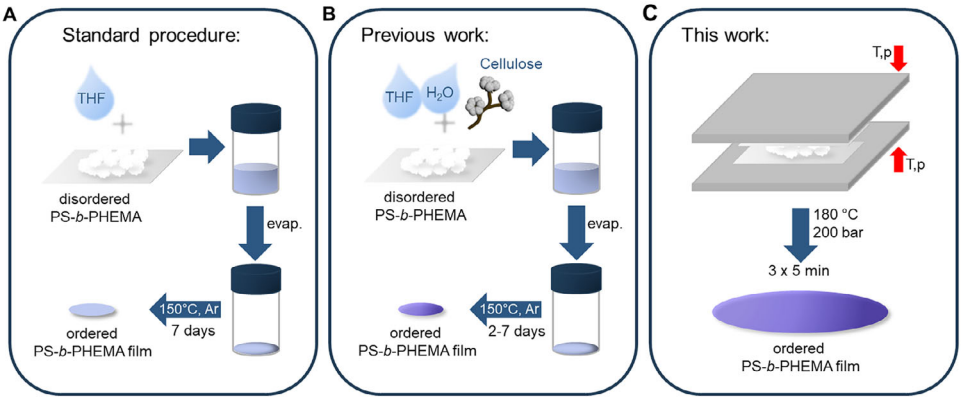

Figure 1. Illustration of three approaches to produce phase-separated bulk films of BCPs. The standard procedure (A) is based on a BCP solution in a suitable solvent followed by solvent evaporation and final thermal annealing of the formed film, which is for PS-*b*-PHEMA 7 d at 150 °C and always results in transparent PS-*b*-PHEMA bulk film. The transparency is shown as light blue. In previous work (B), comparable nanostructures were realized in a shorter time (2 d) by introducing linters fibers,[61] which seems to lower the energy barrier of order-to-order transition (OOT) for HMW PS-*b*-PHEMA.[52] Within this work (C), freestanding films were produced within 15 min by applying pressure and temperature to the pure polymer powder. Final bulk films are represented as purple-bluish to represent the photonic properties of the HMW PS-*b*-PHEMA films.

introduced in 2001 by Ruhl et al.,[62] which was reinvestigated in 2013 by Schäfer et al. for the organization of core–shell colloids to generate photonic elastomer films on a larger scale,[63,64] this technique is investigated in this work for the microphase separation of PS-*b*-PHEMA BCPs. In general, this process is known in materials science as *hot pressing*, which we will refer to in the following discussion.

Within the present work, a solvent-free approach is presented utilizing shear force and pressure as an external trigger to form freestanding photonic material of HMW PS-*b*-PHEMA (Figure 1C). Furthermore, the effect of pressure, temperature and time using the hot pressing method was explored. The resulting microstructures were analyzed by transmission electron microscopy (TEM), scanning electron microscopy (SEM), confocal fluorescence microscopy, and small-angle X-ray scattering (SAXS) measurements. Furthermore, photonic properties were investigated by UV–vis and fluorescence spectroscopy.

2. Results and Discussion

2.1. Polymer Synthesis and Characterization

Amphiphilic BCPs polystyrene-*b*-poly(2-hydroxyethyl methacrylate)s (PS-*b*-PHEMA)s were synthesized by sequential anionic polymerization as given in **Scheme 1** following previous works.[65–67] BCPs with a molecular weight greater than 250 kg mol^{-1} and a PHEMA volume fraction of more than 30 vol%, can only be realized with an excess of 2-(trimethylsilyloxy)ethyl methacrylate (HEMA-TMS) as the kinetic is affected by reduced solubility (Table S1, Supporting Information).

The obtained BCPs and their corresponding PS precursors were characterized with respect to their molar masses using size exclusion chromatography (SEC) measurements and ^{1}H NMR spectroscopy (Table S2, Supporting Information). The successful removal of the trimethylsilane (TMS)-protecting groups by hydrochloric acid resulted in the corresponding amphiphilic PS-*b*-PHEMAs. In this work, the deprotection procedure was slightly modified from earlier reports[61] due to the decreased solubility of the HMW PS-*b*-PHEMA in THF. For this purpose, dimethylformamide (DMF) was added, which promotes the cleavage of silyl ethers[69,70] and increases the solubility of the PHEMA block. Furthermore, a reduced reaction time of 2 h was used to prevent side reactions like cross-linking.

Due to the low solubility of the HMW PS-*b*-PHEMA (M_n > 170 kg mol^{-1} and φ_{PHEMA} >20 vol%) in THF, impurities such as residual monomers, silyl-leaving groups as well as PS homopolymer, could be removed easily by washing the BCP with small quantities of THF (Figures S1 and S2, Supporting Information). This is a great advantage compared to the purification of BCPs with lower molecular weight (<140 kg mol^{-1}). The results on molar masses M_n, $Đ$, and PHEMA volume fractions for all BCPs used in this study are listed in **Table 1**.

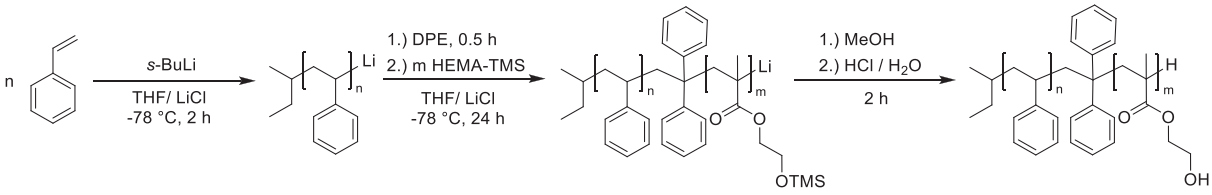

Scheme 1. Synthetic route of PS-*b*-PHEMA by sequential anionic polymerization of styrene and trimethylsilyl-protected 2-hydroxyethyl methacrylate (HEMA-TMS) in tetrahydrofuran (THF) using *sec*-butyllithium (*s*-BuLi) as initiator. Diphenylethylene (DPE) is used as a steric spacer, which reduces reactivity and allows controlled formation of the second block.[68] The hydrolysis of the BCP precursor was carried out in methanol (MeOH), yielding the desired BCP PS-*b*-PHEMA.

© 2025 The Author(s). Advanced Materials Interfaces published by Wiley-VCH GmbH

21967350, 2026, 1, Downloaded from https://advanced.onlinelibrary.wiley.com/doi/10.1002/admi.202500593 by Saarlandische Universitäts- Und Landesbibliothek Sulb, Wiley Online Library on [03/02/2026]. See the Terms and Conditions (https://onlinelibrary.wiley.com/terms-and-conditions) on Wiley Online Library for rules of use; OA articles are governed by the applicable Creative Commons License

Table 1. Characterization data of synthesized PS-*b*-PHEMA BCPs. BCP is given as PS_{76}-*b*-$PHEMA_{24}$ [174]. The subscripts denote the volume fraction in vol%, and the superscript is the corresponding calculated molecular weight in kg mol^{-1}.

	Polymer	$M_{n,SEC}$ [a)] [kg mol^{-1}]	$M_{n,cal}$ [b)] [kg mol^{-1}]	$Đ$ [a)]	$\varphi_{PHEMA,cal}$ [b)] [vol%]
BCP for process optimization—temperature and pressure variation					
1	PS_{70}-*b*-$PHEMA_{30}$ [145]	143	145	1.13	30
2	PS_{69}-*b*-$PHEMA_{31}$ [161]	173	161	1.16	31
BCPs for evaluation of the quality of the hot pressing process					
3	PS_{84}-*b*-$PHEMA_{16}$ [43]	43	43	1.03	16
4	PS_{76}-*b*-$PHEMA_{24}$ [58]	57	58	1.08	24
5	PS_{59}-*b*-$PHEMA_{41}$ [74]	68	74	1.05	41
BCP of investigated polymer films					
6	PS_{60}-*b*-$PHEMA_{40}$ [175]	185	175	1.17	40
7	PS_{49}-*b*-$PHEMA_{51}$ [224]	250	224	1.24	51
8	PS_{48}-*b*-$PHEMA_{62}$ [232]	229	232	1.34	62
9	PS_{58}-*b*-$PHEMA_{42}$ [243]	264	243	1.29	42
10	PS_{52}-*b*-$PHEMA_{48}$ [320]	350	320	1.33	48
11	PS_{83}-*b*-$PHEMA_{17}$ [429]	415	429	1.11	17

[a)] Molecular weight and $Đ$ of PS-*b*-PHEMA determined by SEC in kg mol^{-1} (PMMA standards, DMF); [b)] Molecular weight (in kg mol^{-1}) and volume fraction (in vol%) of the non-styrene block segment calculated by ^{1}H NMR and the molecular weight of the corresponding PS block (M_n, PS block was determined by SEC (PS standards, THF)) with the densities δ_{PS} = 1.05 g mL^{-1},[71] δ_{PHEMA} = 1.15 g mL^{-1}.[72]

Tailored BCPs with molecular weight in the range of 145–429 kg mol^{-1} featuring a PHEMA content of 15–62 vol% have been successfully synthesized by anionic polymerization. The BCPs exhibited well-defined molecular weight distributions with polydispersity index values, $Đ$, ranging from 1.03 to 1.34. The higher $Đ$ values result from the acidic cleavage of PS-*b*-P(HEMA-TMS), which can lead to side reactions, especially with higher PHEMA contents. Nevertheless, good phase separation can still be ensured, demonstrated by the uniform micelle formation (Table S3 and Figure S3, Supporting Information).

Due to its polar hydroxyl groups, PS-*b*-PHEMA shows a tenfold higher Flory–Huggins parameter χ compared to PS-*b*-PMMA.[73,74] Within our previous studies, this property was used for the preparation of PS-*b*-PHEMA membranes by taking advantage of the self-assembly and nonsolvent-induced phase separation (SNIPS) process.[67,75] In addition, phase separation behavior was investigated for PS-*b*-PHEMA BCPs with molecular weight in the range of 40–201 kg mol.$^{-1}$ Here, the estimated χ parameter of Cheng et al. was confirmed with a value of 0.37,[73] which is comparable to the high χ parameter of PS-*b*-P4VP (χ = 0.30–0.40).[76,61] The introduction of linters fibers to the standard solution-based approach (Figure 1B) accelerated phase separation due to interfacial forces, particularly for high molecular weight PS-*b*-PHEMA, leading to a bluish bulk film for PS_{72}-*b*-$PHEMA_{28}$ [201], which shows angle-dependent optical properties.

2.2. Evaluation of Hot Pressing Parameters

In the following, the microphase separation was investigated as a function of temperature, pressure, and time using the hot pressing method (Figure 1C) with the polymers PS_{70}-*b*-$PHEMA_{30}$ [145] and PS_{69}-*b*-$PHEMA_{31}$ [161] to obtain comparable optoelectronic properties without the use of an additive. To compare both approaches, the molecular weights and PHEMA volume fractions of the BCPs are in the range of the PS_{72}-*b*-$PHEMA_{28}$ [201] used in our previous study, which exhibited photonic properties as mentioned earlier.[61] The microstructure is affected mostly by the temperature as the phase separation correlates with the polymer chain dynamic. In general, temperatures significantly higher than the glass transition temperatures T_g of the polymer segments were applied to ensure sufficient chain mobility. Both BCPs show the highest T_g at around 122–123 °C (Figure S4, Supporting Information), referring to the PHEMA segment. Thus, the investigated temperatures ranged from 125 to 200 °C, limited by the thermal stability of the polyethylene terephthalate (PET) protective foil. The use of elevated temperatures alone was insufficient to enable adequate chain mobility of the HMW PS-*b*-PHEMA, as described previously.[61]

Shear forces were introduced by applying a pressure of 50 bar to provoke shear-thinning.[35,77] To provide an idea of the chain mobility, the memory and loss modulus, as well as the complex viscosity of intermediate and high molecular weight PS-*b*-PHEMA BCPs, are shown in **Figure 2A**. The investigation of the viscoelastic properties underlines the desired shear-thinning characteristic.

The phase separation of BCP PS_{70}-*b*-$PHEMA_{30}$ [145] was investigated at 125 °C and from 150 to 200 °C in 10 °C steps (Figure S5, Supporting Information). Figure 2B shows TEM images of the obtained microstructure after hot pressing treatment at a constant pressure of 50 bar for 5 min at 125, 150, 180, and 200 °C. The TEM images clearly demonstrate the evolution of a microstructure with increasing temperature. Starting at 125 °C near the T_g of around 120 °C, no clear phase separation was obtained, but the first separation features are visible in lighter and darker areas. The light areas correspond to PHEMA and the dark areas to PS domains. At 150 °C, a clear microstructure is visible, but the boundaries show soft contours. In our experience, this temperature is suitable for the long-term annealing of BCP films,[61,67,73] as it is not affected by the thermal aging of the polymer film due to degradation and cross-linking reactions that can occur above 200 °C.[78] Above 160 °C, no significant change in phase separation is visible based on TEM investigations, and only small differences in the dimensions of the resulting film can be recognized (Figure S5, Supporting Information). SAXS experiments, to investigate the bulk structure of the films, provide similar results (Figure 2C). At 125 °C, a single weak shoulder at 0.005 Å^{-1} is present, indicative of a homogeneous structure on nanometer length scales. At 150 °C, this shoulder has become more pronounced, and a second weak shoulder is present at 0.02 Å^{-1}. It shows that well-defined domains with sizes of ~100 nm become present, as is also apparent from TEM. At 180 and 200 °C, a structure factor peak at 0.005 Å^{-1} emerges, showing that the spacings between domains become uniform, and no significant structural change is observable between the last two temperatures (Figure 2C). To ensure sufficient mobility of higher molecular weight polymer chains and best phase separation, a temperature of 180 °C was used for future investigations. Due to the short-term processing, aging process can be neglected, as proven by the stable viscoelastic properties even after 10 runs of frequency

© 2025 The Author(s). Advanced Materials Interfaces published by Wiley-VCH GmbH

21967350, 2026, 1, Downloaded from https://advanced.onlinelibrary.wiley.com/doi/10.1002/admi.202500593 by Saarlandische Universitäts- Und Landesbibliothek Sulb, Wiley Online Library on [03/02/2026]. See the Terms and Conditions (https://onlinelibrary.wiley.com/terms-and-conditions) on Wiley Online Library for rules of use; OA articles are governed by the applicable Creative Commons License

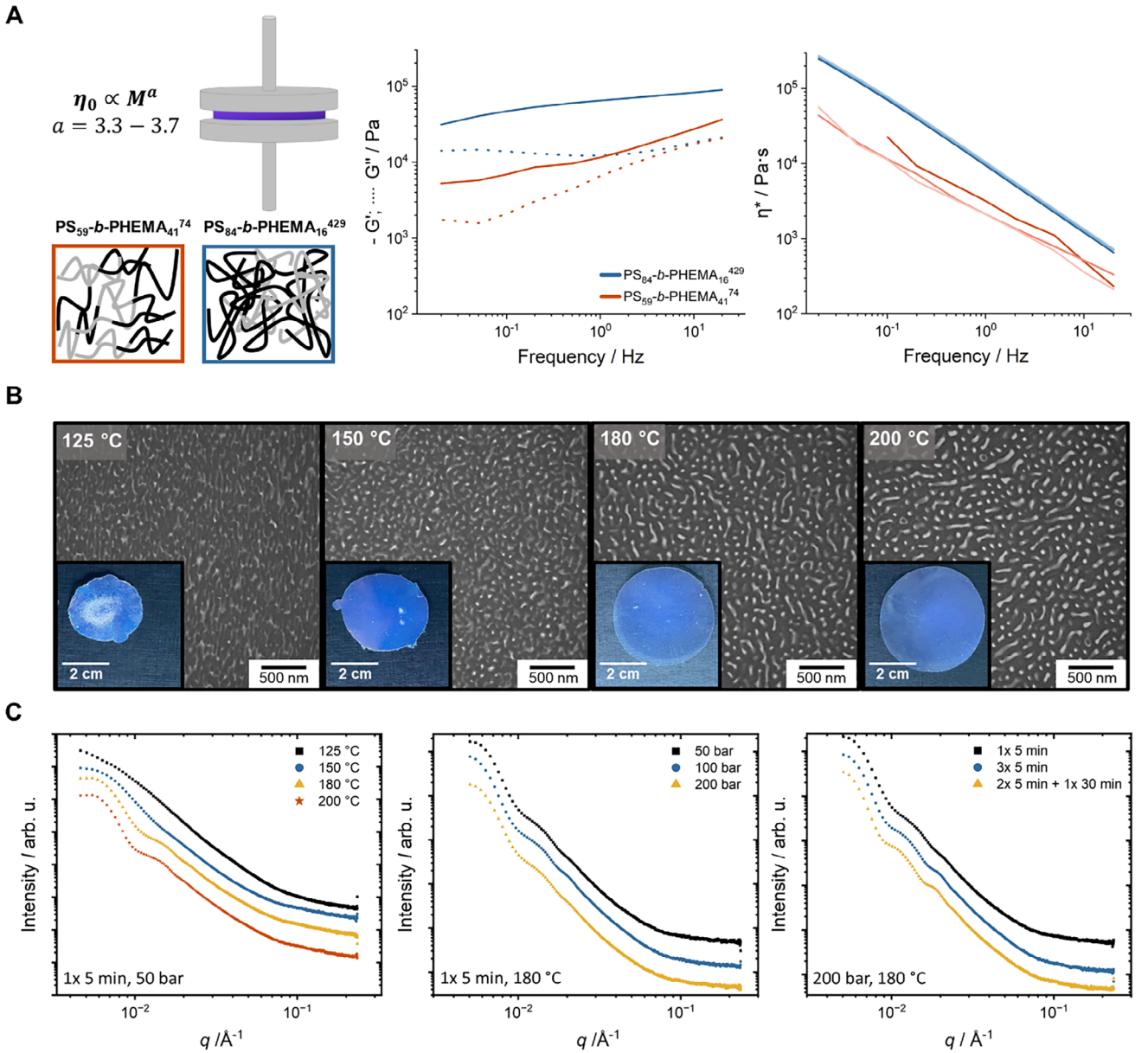

Figure 2. Evaluation of the process parameters for a sufficient phase separation process via the hot pressing method using PS-*b*-PHEMA BCPs by variation of temperature, pressure, as well as number of cycles. A) Dynamic mechanical analysis (DMA) using PS_{59}-*b*-$PHEMA_{41}$ [74] (intermediate molecular weight; orange) and PS_{84}-*b*-$PHEMA_{16}$ [429] (HMW; blue) showing *G′* (bold; run 10) and *G″* (dotted; run 10) in dependence of frequency and complex viscosity *η** (run 1, 5, and 10; dark to light) giving hint of the chain dynamic in melt state at 180 °C. B) Characteristics of the macroscopic appearance of the BCP film shown by means of photography as well as microstructures, determined by TEM for temperature variation using PS_{70}-*b*-$PHEMA_{30}$ [145] and C) SAXS patterns of PS-*b*-PHEMA films after hot pressing with varying temperatures (left panel; PS_{70}-*b*-$PHEMA_{30}$ [145]), varying pressures (middle panel; PS_{69}-*b*-$PHEMA_{31}$ [161]), and varying cycles and durations (right panel, PS_{69}-*b*-$PHEMA_{31}$ [161]) using protocols as indicated in the graphs.

sweep from 20 to 0.02 Hz at 180 °C (Figure 2A). Following, the influence of pressure at a set temperature of 180 °C was investigated using BCP PS_{69}-*b*-$PHEMA_{31}$ [161], starting at a pressure of 50 bar and increasing stepwise by 25 bar up to 200 bar. Within this test series, at all pressures, the dimension of the polymer films, as well as the obtained microstructure investigated by TEM and SAXS, remains similar to that of the BCP PS_{70}-*b*-$PHEMA_{30}$ [145], showing no significant difference at 180 °C and 50 bar (Figure 2C and Figure S6, Supporting Information). To introduce the highest shear force, a pressure of 200 bar was used for further investigations. Finally, the time by a number of cycles was examined, whereby the film formed with the hot press was folded for the next cycle. Assuming that melting predefined BCP structures leads to better phase separation, the microstructure was investigated after 1 cycle of 5 min treatment at 180 °C and 200 bar, and after 3 cycles of 5 min each. As the equilibrium of dynamic systems was often reached after longer annealing times, the microstructure was also investigated after 2 cycles of 5 min and a

© 2025 The Author(s). Advanced Materials Interfaces published by Wiley-VCH GmbH

21967350, 2026, 1, Downloaded from https://advanced.onlinelibrary.wiley.com/doi/10.1002/admi.202500593 by Saarlandische Universitats- Und Landesbibliothek Sulb, Wiley Online Library on [03/02/2026]. See the Terms and Conditions (https://onlinelibrary.wiley.com/terms-and-conditions) on Wiley Online Library for rules of use; OA articles are governed by the applicable Creative Commons License

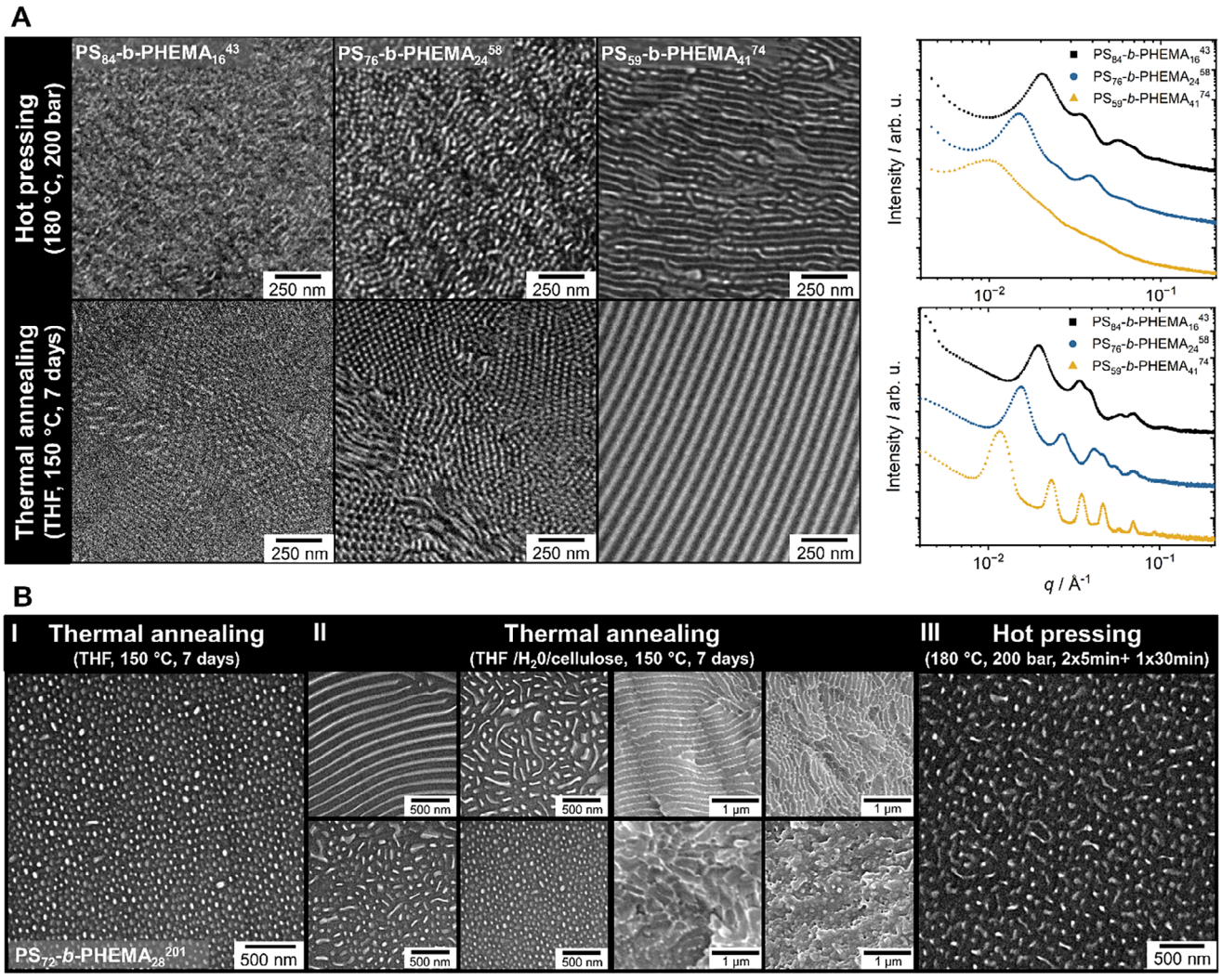

Figure 3. Evaluation of the performance of different approaches for the evolution of microstructures by comparing the obtained morphology of PS-*b*-PHEMA BCPs. A) Comparison of the microstructure of intermediate molecular weight PS-*b*-PHEMA (<100 kg mol^{-1}) obtained by hot pressing and solvent-based processing using TEM and SAXS investigations. B) Observation of the phase separation of HMW PS_{72}-*b*-$PHEMA_{28}{}^{201}$, which exhibits a trapped spherical microstructure when prepared from a THF solution (I, TEM images). By adding a cellulose/water mixture to the THF, a heterogeneously structured bulk film is obtained (II, TEM images with 500 nm scale bar and SEM images of equivalent regions with 1 µm scale bar showing broader region). Finally, the hot pressing process resulted in a homogeneous, isotropic, freestanding film with a bicontinuous nanostructure (III, TEM images).

final run of 30 min. TEM investigations indicate no significant change in microstructure (Figure S7, Supporting Information). Only the SAXS measurements (Figure 2C) indicated that structural characteristics change from 1 to 3 cycles by showing more distinct reflexes for higher cycle numbers and slightly changed positions. The third method, with 2 cycles of 5 min and a final for 30 min, resulted in comparable structural characteristics as for processing 3 times for 5 min. For further investigation, a standard hot pressing protocol was employed, in which the polymer was treated at 180 °C and a pressure of 200 bar for 2 cycles of 5 min and 1 cycle of 30 min.

Besides providing a different processing approach to generate PS-*b*-PHEMA microstructured films, this work also directly compares the hot pressing method with the published solvent-based procedures (Figure 1).[67] For this purpose, the low molecular weight BCPs PS_{84}-*b*-$PHEMA_{16}{}^{43}$, PS_{76}-*b*-$PHEMA_{24}{}^{58}$, and PS_{59}-b-$PHEMA_{41}{}^{74}$, which were investigated in previous work,[61] were processed with the evaluated hot pressing protocol. The obtained characteristics of the microstructures were investigated using TEM and SAXS and compared to those of the solution-based procedure, as shown in **Figure 3A**. A comparison of the TEM images shows no pronounced effect of the two different methods on the sizes and morphology of the resulting PS and PHEMA domains. However, a significant difference in the long-range order of the resulting microstructure was observed. This is clearly identified by a closer look at both lamellar structures, where the solvent-based process led to a long-range lamellar structure of up to 10 µm (Figure S8, Supporting Information). In contrast, the hot pressing process led to a pre-oriented intercrossing lamellar structure where the long-range order is below 250 nm, defined by a lamellar area with no broken line. These findings, which represent only a small area of the sample examined with TEM, were

© 2025 The Author(s). Advanced Materials Interfaces published by Wiley-VCH GmbH

21967350, 2026, 1, Downloaded from https://advanced.onlinelibrary.wiley.com/doi/10.1002/admi.202500593 by Saarlandische Universitäts- Und Landesbibliothek Sulb, Wiley Online Library on [03/02/2026]. See the Terms and Conditions (https://onlinelibrary.wiley.com/terms-and-conditions) on Wiley Online Library for rules of use; OA articles are governed by the applicable Creative Commons License

21967350, 2026, 1, Downloaded from https://advanced.onlinelibrary.wiley.com/doi/10.1002/admi.202500593 by Saarlandische Universitäts- Und Landesbibliothek Sulb, Wiley Online Library on [03/02/2026]. See the Terms and Conditions (https://onlinelibrary.wiley.com/terms-and-conditions) on Wiley Online Library for rules of use; OA articles are governed by the applicable Creative Commons License

also confirmed for the bulk structure by SAXS measurements. Figure 3A shows that, for the PS_{59}-*b*-$PHEMA_{41}$[74] BCP film after thermal annealing, pronounced Bragg peaks are present at relative positions corresponding to a lamellar structure.[79] Contrary, the same sample after hot pressing only shows a weak primary structure factor peak with very weak shoulders at positions consistent with a lamellar structure. This indicates microphase-separation of the block copolymers into weakly defined lamellar structures. For both PS_{84}-*b*-$PHEMA_{16}$[43], PS_{76}-*b*-$PHEMA_{24}$[58], the scattering patterns of the samples prepared with both processing methods show a series of pronounced Bragg peaks at positions consistent with a hexagonal morphology.[79] The peaks measured using the thermally annealed sample, however, are slightly more pronounced, indicating better long-range order, consistent with the observations from TEM. Furthermore, the microstructure evolution of the high molecular PS-*b*-PHEMA with photonic properties from our previous work[61] was investigated by the hot pressing process and was compared with the microstructure obtained by the solvent-based processes (Figure 3B). The standard THF solution resulted in densely packed spherical micellar structures that were unable to overcome the interfacial tension. By adding linters fibers to the solution, surface forces directed the self-assembly of the polymer chains, resulting in an inhomogeneous bulk film that ranged from spherical to bicontinuous to lamellar structures. The volume fraction of PHEMA with 28% theoretically leads to an equilibrium structure between cylindrical and lamellar structures.[11,61] As the PHEMA volume fraction is below 35%, the fiber-induced lamellar structure transformed into a bicontinuous structure with minimized packaging frustration. Nevertheless, an energetically restricted spherical structure was still observed, which suggests that no long-range forces were present. In contrast, the hot pressing process led to a homogeneous freestanding film, showing an irregular but well-pronounced nanostructure with comparable features to the bicontinuous structure of the film with linters fiber. Due to the SSL regime, no intermediate equilibrium structure like O_{70} or gyroid structure is expected and observable according to self-consistent field theory (SCFT).[14,80,81] Furthermore, SCFT also predicts a spherical phase as a separation phase between the other equilibrium phases and the disordered phase, which discriminates fluctuation effects and corresponds to $\bar{N} \rightarrow \infty$.[14] The evolution time of an equilibrium state is always associated with the chain mobility and therefore with the viscosity of the polymer melt. Here, the mechanical analysis of PS-*b*-PHEMA BCPs, with intermediate and high molecular weights, shown in Figure 2A, indicates a significant increase in viscosity by about one order of magnitude due to the pronounced entanglement of polymer chains with increasing molecular weight. Crossing energy hurdles, therefore, requires more energy or external forces for HMW BCPs. Without this additional force, the morphologies are trapped in the spherical micellar structure as the most accessible and stable morphology, which was shown experimentally and is in agreement with the SCFT and the SSL regime.[14,80,81] In general, due to the long relaxation time of HMW BCPs the thermodynamically preferred morphology may only be accessible after a very long time or is not realizable at all from a kinetical point of view, based on Semenov.[52]

Interestingly, the BCP film generated by hot pressing showed the desired photonic properties which were already recognized by the nanostructure generated in the vicinity of cellulose, despite the absence of a lamellar structure.[61] Overcoming the thermodynamically trapped spherical structure is enabled on the one hand by the hot pressing process resulting in freestanding BCP films with hexagonally packed cylinders, bicontinuous and kind of lamellar structures (**Figures 4** and S9, Supporting Information). This structural change is also visible to the naked eye: first, a transparent film is obtained using the standard process (spherical structure), followed by a bluish photonic film through the addition of cellulose (lamellae/network/spheres),[61] which ultimately leads to a freestanding transparent violet film using the hot pressing method (disordered network structure) (Figure S10, Supporting Information). On the other hand, the solution-based process could also be improved by using a solvent mixture of THF and DMF (10/1 v/v), where DMF acts as an interfacial active and PHEMA-selective substance. By this, clear lamellar structures were obtained, whose long-range order could be again improved by adding linters cellulose (see Figure S11, Supporting Information). The investigated PS_{60}-*b*-$PHEMA_{40}$[175] shows a bicontinuous structure with increased lamellar features in comparison to the obtained structure of PS_{72}-*b*-$PHEMA_{28}$[201] (Figure 3B). Further optimization to achieve a long-range ordered thermodynamic equilibrium microstructure of the HMW block copolymer could be possible by applying currently promising concepts to BCPs with M_n <100 kg mol^{-1}, like the shear-rolling process[82–84] with more focus on shear forces[85] or the usage of momentary thickness gradients.[86] A scale-up approach has already been demonstrated in previous work, using the melt shear process to form colloidal opal films from polymer powder.[87] Due to the comparable behavior of the BCP during processing, transfer to the BCP hot press process is possible, although adjustments using manufacturing additives may be necessary.

2.3. Characterization of Photonic BCP Films

So far, a solvent-free approach for the preparation of nanostructured, freestanding polymer films of HMW PS-*b*-PHEMA within 15 min that exhibit photonic properties has been presented in this work. In the following, the nature of the photonic properties will be investigated as photonic materials based on diblock copolymers with anisotropic interpenetrating systems or lamellar structures are rarely described in the literature. In contrast, spherical structures are excellently covered by colloidal polymer systems.[33] Thus, the focus here is on HMW PS-*b*-PHEMA with higher PHEMA volume ratios (>40 vol%), with the microstructural regime ranging from bicontinuous to lamellar structure, which is in agreement with previous work and the basic literature.[11,61] **Figure 4**A summarizes structural features determined by TEM and SEM as well as confocal fluorescence microscopy. It could be observed that with increasing molecular weight, a change in color of the freestanding film could be recognized, which comprises purple up to light greenish. The greater the difference in aspect ratio of the domains, the more scattering is observable, resulting in decreased transparency and less brilliance of color. This increasing irregularity of structure was visualized by a fast Fourier transform (FFT) representation of processed TEM images, using ImageJ, which revealed a more diffuse pattern. Interestingly, less coloration and greater

 © 2025 The Author(s). Advanced Materials Interfaces published by Wiley-VCH GmbH

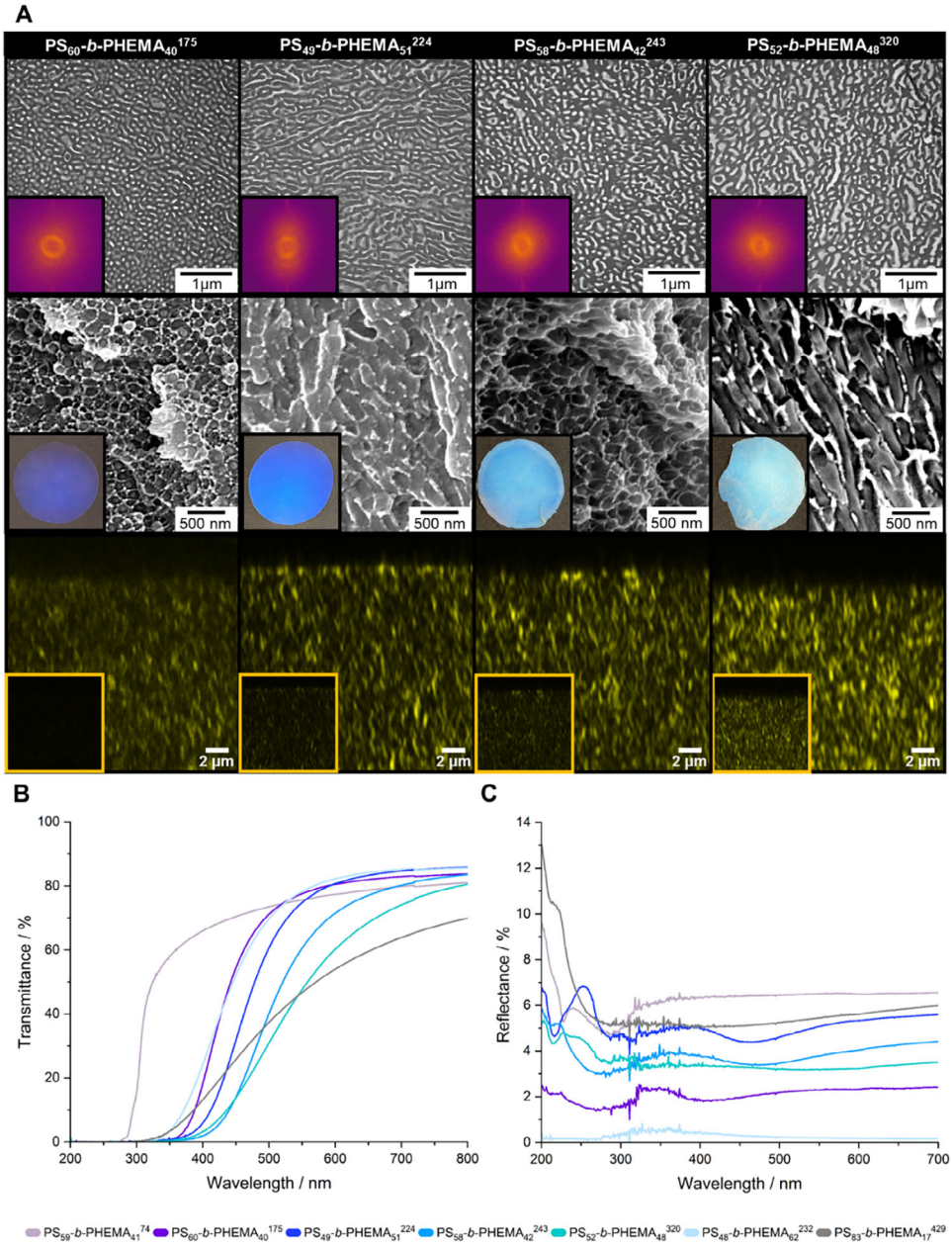

Figure 4. A) Investigation of the microstructure of PS-*b*-PHEMA BCPs using TEM measurements, showing the PHEMA domain in light and the PS domain in dark with related FFT images obtained by ImageJ (first row), SEM measurements with PHEMA in dark and PS in light with the respective image of the colored freestanding polymer film (second row) and confocal fluorescence microscopy of BCP films with more pronounced interconnected lamellar structures exhibited increased fluorescence, as shown in the smaller insets. Intensities in the larger images, on the other hand, were optimized to reveal structural details (third row). B) UV–vis spectra in transmission (left) and reflection mode (right, incident and reflection angle of 10° using Universal Measurement Accessory (UMA)).

transparency were observed for BCPs as PS_{48}-b-$PHEMA_{62}^{232}$ with PHEMA volume ratio higher than 50 vol% (Figure S12, Supporting Information). Furthermore, SEM images indicated interconnected networks of a more hexagonal nature with a lower PHEMA ratio for PS_{60}-*b*-$PHEMA_{40}^{175}$ and PS_{58}-*b*-$PHEMA_{42}^{243}$ to more woven lamellar structure for PS_{49}-*b*-$PHEMA_{51}^{224}$ and PS_{52}-*b*-$PHEMA_{48}^{320}$. In addition, the fluorescence properties of the polymer films were investigated using confocal fluorescence microscopy, as depicted in Figure 4A (third row). BCP films with more pronounced interconnected lamellar structures exhibited increased fluorescence in the high-resolution Z-stack examinations. The fluorescent areas refer to the PHEMA domain, which was confirmed by staining with rhodamine B methanol solution (Figure S13, Supporting Information). Intrinsically, the homogeneous distribution of rhodamine B in the fluorescent domain confirmed the interconnected system, as the solution

© 2025 The Author(s). Advanced Materials Interfaces published by Wiley-VCH GmbH

21967350, 2026, 1, Downloaded from https://advanced.onlinelibrary.wiley.com/doi/10.1002/admi.202500593 by Saarlandische Universitats- Und Landesbibliothek Sulb, Wiley Online Library on [03/02/2026]. See the Terms and Conditions (https://onlinelibrary.wiley.com/terms-and-conditions) on Wiley Online Library for rules of use; OA articles are governed by the applicable Creative Commons License

Table 2. Characteristics of films, manufactured by hot pressing method, giving the detected reflection wavelength area $\lambda_{refl.}$ as well as the volume fraction of the PHEMA block and its Feret length, with min. Feret length in brackets, for the description of the structural features observed by TEM investigations (statistical values are given in Table S4, Supporting Information). The number in brackets of the $\lambda_{refl.}$ refers to the wavelength showing the maxima in reflectance, which was converted to a mains level spacing of $a_{\lambda\ refl.}$ (Figure S15, Supporting Information) using Bragg's law with the effective refractive index n_{eff} using n_{PS} = 1.59[91] and n_{PHEMA} = 1.44[92] according to literature.[93]

#	Polymer	$\lambda_{refl.}$ [nm]	$a_{\lambda\ refl.}$ [nm]	φ_{PHEMA} [vol%]	$d_{F,PHEMA}$ [nm]
3	PS_{59}-*b*-$PHEMA_{41}^{74}$	229–287 (239)	102.5	42	54.7 (10.3)
7	PS_{60}-*b*-$PHEMA_{40}^{175}$	272–404 (325)	139.1	42.9	115.5 (63.2)
10	PS_{49}-*b*-$PHEMA_{51}^{224}$	216–287 (252) 289–462 (381)	108.7 164.4	47.6	183.0 (58.7)
11	PS_{48}-*b*-$PHEMA_{62}^{232}$	275–495 (374)	160.1	44.8	189.2 (89.2)
12	PS_{58}-*b*-$PHEMA_{42}^{243}$	229–270 (225) 288–466 (374)	82.9 158.9	36.2	154.2 (81.9)
16	PS_{52}-*b*-$PHEMA_{48}^{320}$	281–311 (227) 326–533 (403)	97.7 173.6	46.4	196.6 (98.8)
18	PS_{83}-*b*-$PHEMA_{17}^{429}$	213–269 (214)	87.5	13.6	61.2 (37.9)

selectively penetrates into the PHEMA domain and does not interact with the PS matrix. To trace the origin of the photonic properties, UV–vis and fluorescence spectroscopic investigations were conducted. Figure 4B displays the transmission spectra of selected BCPs, which show overall decreasing transparency by increasing molecular weight. At the same time, the transmitted light shifts to higher wavelengths. The polymer films showed absorption edges comparable to semiconductors or metals and are, therefore, impermeable to wavelengths below the photonic bandgap. Thus, the hot pressing method resulted in freestanding BCP films with tailored photonic bandgaps, which in the case of the PS_{60}-*b*-$PHEMA_{40}^{175}$ film are impermeable to UV light, and in the case of the PS_{52}-*b*-$PHEMA_{48}^{320}$ film, even up to wavelengths of the green spectrum. In addition, the reflection spectra (Figure 4C) show at lower reflection angles (<± 35°) the expected wavelengths, which were already visible to some extent with the eyes (Figure S14, Supporting Information). As the microstructures are not perfectly aligned and the difference in the refractive index of the polymer domains is low (≈0.15), the structural color is less pronounced.

To substantiate the above-described photonic properties, the maximum wavelength of the reflection color extracted from UV–vis spectra in reflection mode, which was supported by the absorption spectra of the films, was transferred to a structural dimension (**Table 2**). These were compared to the size of the structural features, derived by the imaging analysis of the TEM measurements using ImageJ (Figure S3, Supporting Information). Thus, the definition of a structural dimension is challenging due to its interpenetrating character; micellar dimensions were also provided for both dry and swollen states to give an overall view (Table S3 and Figure S3, Supporting Information). In general, the dimensions of the structural features are in the range of the observed wavelength maxima, which supports the assumption of the appearance of a structural color. The relationship between color and structural dimension could also be shown by the work of Karaman et al., showing a Bragg mirror using PHEMA and titanium dioxide with similar spacings.[88] Also worth mentioning is that photonic properties were only recognizable for PS-*b*-PHEMA BCP with PHEMA volume fractions higher than 20 vol % up to ≈60 vol%, which is also a hint for a photonic bandgap.[22] In addition, circular-disk and elliptical-disk like FFT spaces could be shown for the domain arrangement of the microstructures processed from TEM images with ImageJ (FFT images Figure 4A). Considering recent works that have dealt with disordered hyperuniform structures and their Fourier-space exclusion regions as well as their optoelectronic properties, it is assumed that in this work, disordered hyperuniform structures were obtained from the polymer melt in 2D confinement, which exhibit photonic bandgaps.[29,42,44,45,89] An additional indication for such a disordered hyperuniform structure is the homogeneous isotropic structure of the film, which has no grain boundaries, whereas this is often the case for solvent-based BCP films (Figure S11, Supporting Information).[29,90]

In addition to the standard UV–vis measurements, investigations of angle-dependent reflection with *s*- and *p*-polarized as well as non-polarized light were conducted. In general, the structural color diminished as the incident angle increased using non-polarized light. Simultaneously, features in the UV region are getting more pronounced. By using polarized light, structural color was still visible even with higher incidence angle, but a shift to lower wavelengths at increasing angles was observable. Although *s*- and *p*-polarized light do not differ much at low incidence angles, clear differences were recognized at higher angles, leading to increased reflection of p-polarized light and no reflection of *s*-polarized light below 240 nm, which indicates that the light is affected by the structural features of the film. As the PS_{49}-*b*-$PHEMA_{51}^{224}$ film shows most clearly the photonic nature, this behavior will be demonstrated based on this freestanding polymer film in the supporting information (Figure S16, Supporting Information).

As aromatic and polar polymers tend to show fluorescence, due to aggregation-induced emission (AIE) for extended π-conjugated structures, clusterization-triggered emission (CTE) for electron-rich units like PS or heteroatoms,[94] the fluorescence of the freestanding films were investigated. **Figure 5** shows the obtained excitation and emission spectra of the polymer powders and the freestanding films. In general, it is observable that the excitation bands of PS powder differ only in the band around 290 nm from the PS-*b*-PHEMA powder (Figure 5, left). All investigated samples show only strong excitation for wavelengths below 300 nm, as shown by a second scan from 285 to 540 nm illustrated by dashed lines. Interestingly, the excitation spectra of the films show additional features in the 290–325 nm range. Furthermore, the excitation spectra depend on the microstructure of the polymer film, which is clearly visible by comparing the co-continuous system PS_{49}-*b*-$PHEMA_{51}^{224}$ with the cylindrical structure of PS_{83}-*b*-$PHEMA_{17}^{429}$. Herein, the excitation decreases for the cylindrical nanostructure drastically, suppressing the fluorescence of the PS. Moreover, µm thick films of intermediate molecular weight BCPs (<100 kg mol^{-1}) like PS_{59}-*b*-$PHEMA_{41}^{74}$, showed the lowest intensity of fluorescence, possessing only a low level of fluorescence of the BCP powder with less pronounced PS region like PS_{83}-*b*-$PHEMA_{17}^{429}$. The fluorescence spectra in

© 2025 The Author(s). Advanced Materials Interfaces published by Wiley-VCH GmbH

21967350, 2026, 1, Downloaded from https://advanced.onlinelibrary.wiley.com/doi/10.1002/admi.202500593 by Saarländische Universitäts- Und Landesbibliothek Sulb, Wiley Online Library on [03/02/2026]. See the Terms and Conditions (https://onlinelibrary.wiley.com/terms-and-conditions) on Wiley Online Library for rules of use; OA articles are governed by the applicable Creative Commons License

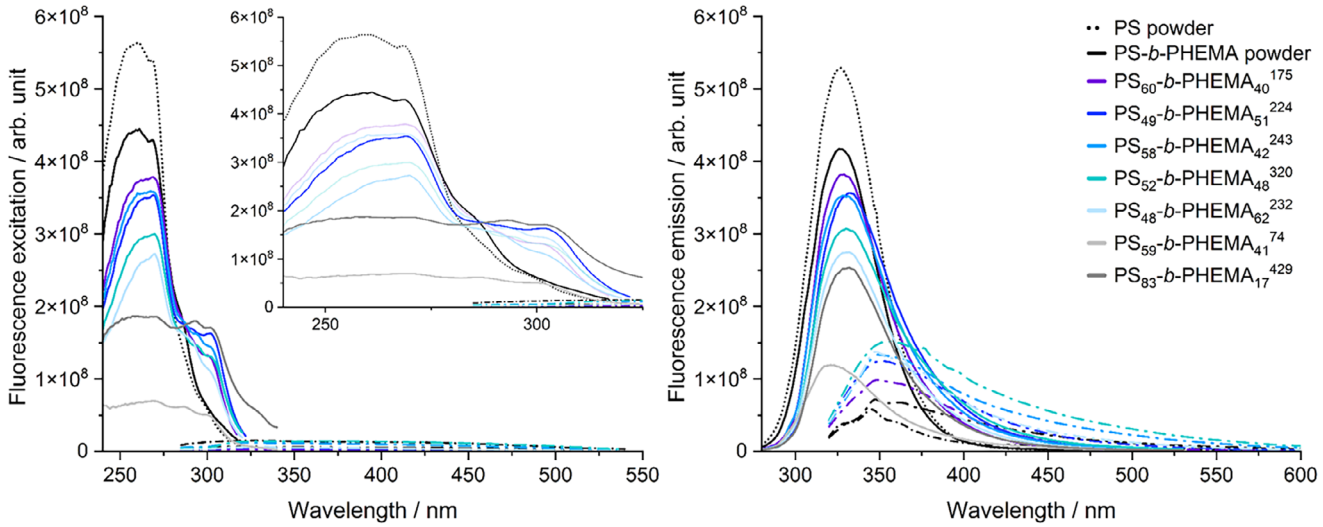

Figure 5. Characteristic fluorescence properties of PS-*b*-PHEMA films shown by excitation spectra (left) observing wavelength region of 240–317 nm (bold) and 285–540 (dashed) and emission spectra (right) by excitation with a wavelength of 270 nm (bold) and 310 nm (dashed). Zoom-in of the excitation spectra highlights the different features due to microstructure compared to the polymer powder (black lines).

Figure 5 (right) show the emission of the polymer powders and freestanding films using an excitation wavelength of 270 nm (bold) and 310 nm (dashed). A distinct emission with a Gaussian distribution was observed for the powders at an excitation wavelength of 270 nm. In contrast, for microstructured films, a slight shift to higher wavelengths and a subsequent tailing of the emission spectrum were obtained, uniquely for each film. The excitation with a wavelength of 310 nm also leads to distinct emission with a greater tailing of the spectra (Figure 5, right), which is predominantly related to the PHEMA, as the emission of PS powder ends at a much lower wavelength than for the BCP powder. The higher emission for the BCP films compared to the BCP powder and the massive tailing effect support the assumptions of CTE due to PHEMA domains, which would be in line with the investigations by the confocal fluorescence microscopy at a wavelength higher than 360 nm. Furthermore, it is worth to note that BCP PS_{48}-*b*-$PHEMA_{62}^{232}$, with the highest content of PHEMA, also shows a decrease in emission wavelength.

In summary, the photonic effect is as complex as the structure of the freestanding BCP films. Photonic properties recognizable by the eye were only obtained with PHEMA ratios from 20 up to 62 vol%, with co-continuous structures. The visual effects have been proven by the investigation of absorption, fluorescence, and reflection. The weak coloration of the films can be referred to as structural color, as the reflection spectra confirm weak bands at expected wavelength regions, which should not be much affected by fluorescence, as the spectra were measured from high to low wavelength regions. The intensity of color is in line with the expectations according to Fresnel,[93] referring to a low difference in refractive index of 0.15 and not perfectly aligned structure. The visible luminescence effect can be attributed to fluorescence based on the CTE of PS and PHEMA, but only in the mentioned BCP composition, which indicates a codependency of microstructure, polymer composition, and fluorescence phenomena. These correlations suggest complex interactions between different energy levels, supporting the assumption of photonic bandgap formation, which needs to be investigated in future work through simulations of HMW block copolymers under 2D confinement and 3D structural analyses.[22,44,95] The co-continuous PS-*b*-PHEMA films act as UV and blue light filters for wavelengths up to 450 nm, as shown by the angle-dependent transmission spectra and the great transparency of the film (Figure S17, Supporting Information), thanks to the low refractive index difference. A comparable structure made of silicon dioxide and air, which has a significantly higher refractive index difference of 0.45, results in a sapphire blue structural color that has been compared to the back plumage of the male bluethroat, as recently reported in the literature.[96] Unfortunately, due to kinetic restrictions in polymer synthesis, higher wavelength regions cannot be addressed currently. Furthermore, achieving higher wavelength colors with great color purity using isotropic disordered structures is, from a physical point of view, challenging to realize, as reported.[97]

2.4. Solvent-Responsive Photonic BCP Film

In the following, the application of the investigated photonic materials is the focus. Photonic materials play a crucial role in various application fields, including sensors, optical filters, and dispersion modulation. Therefore, photonic films having an interconnected structure were considered as solvent-selective sensors for polar PHEMA-selective solvents. Due to the interconnected system, fast and homogeneous infiltration of the polymer films by solvents is possible. In this work, a solvent-selective color change of the photonic polymer films (**Figures 6** and S18, Supporting Information), which is reversible using polar and PHEMA-selective solvents, was demonstrated. Due to the refractive index of the pure solvent and its characteristic swelling capacity of the PHEMA domain, a solvent-selective color was achieved that differs significantly from one another. The hot pressing BCP film PS_{49}-*b*-$PHEMA_{51}^{224}$ was chosen as the best

© 2025 The Author(s). Advanced Materials Interfaces published by Wiley-VCH GmbH

21967350, 2026, 1, Downloaded from https://advanced.onlinelibrary.wiley.com/doi/10.1002/admi.202500593 by Saarlandische Universitäts- Und Landesbibliothek Sulb, Wiley Online Library on [03/02/2026]. See the Terms and Conditions (https://onlinelibrary.wiley.com/terms-and-conditions) on Wiley Online Library for rules of use; OA articles are governed by the applicable Creative Commons License

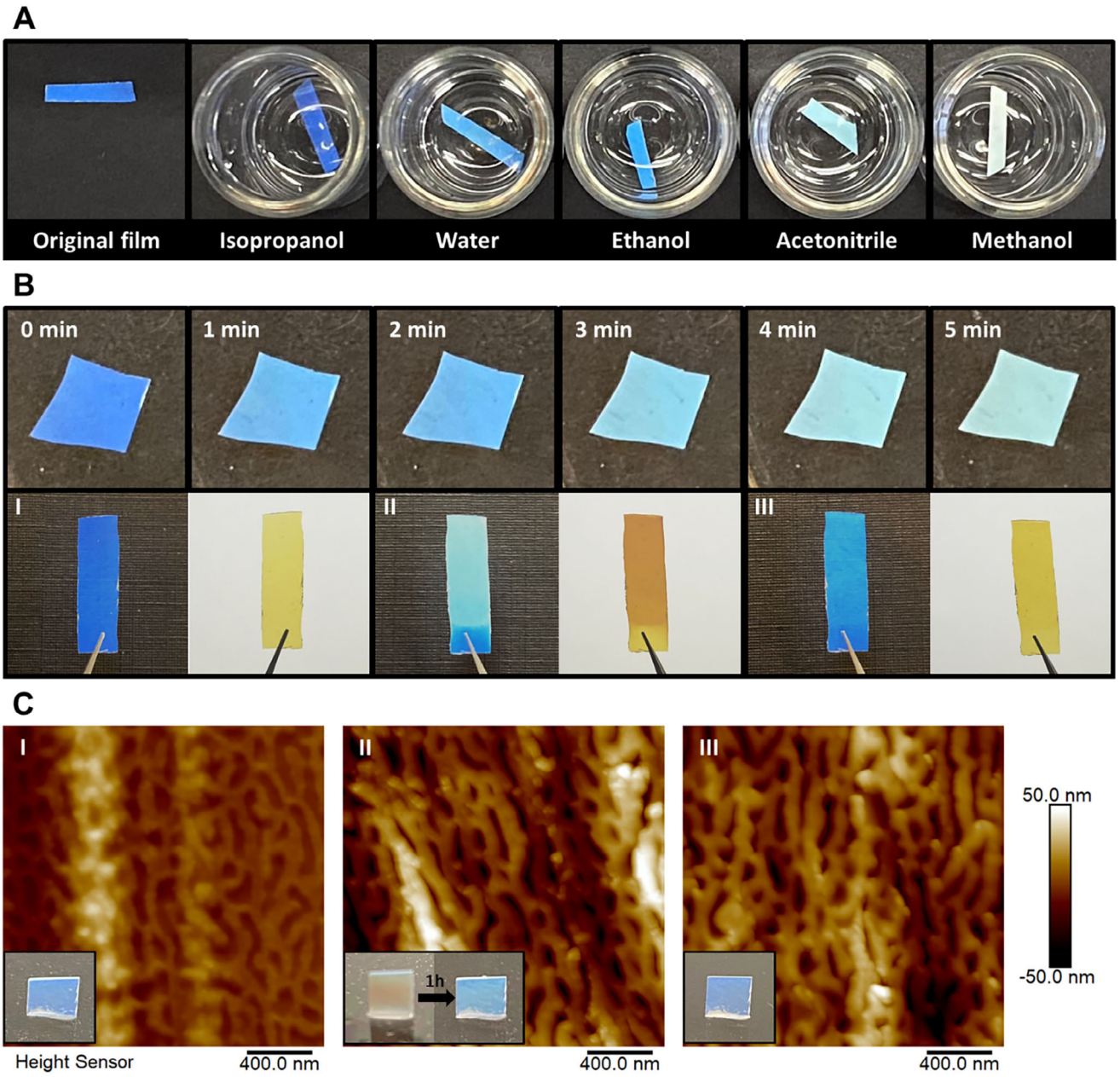

Figure 6. Illustration of the solvent-responsive behavior of the PS-*b*-PHEMA polymer films. A) Color change of PS_{49}-*b*-$PHEMA_{51}^{224}$ film after immersion in different polar solvents like isopropanol ($n = 1.38$), water ($n = 1.33$), ethanol ($n = 1.36$), acetonitrile ($n = 1.34$), and methanol ($n = 1.33$) for 30 min.[98] B) Visualization of the penetration progress of methanol for the initial 5 min based on the color (upper row) and the reversible behavior of this progress shown in the top and through-view of the film in the original (I), swollen (II, 5 min in methanol), and dried (III, 5 min at ambient conditions) state (lower row). C) AFM height profiles in tapping mode showing the initial cross section of the BCP film (I) compared to dried ones after 1 h of immersing the film in methanol and drying for 3 h (II) and overnight (III) with images of the appearance of the film at different time points.

representative due to its clearly visible blueish structural color (Figure S17, Supporting Information). Figure 6 displays the color and structural change of the polymer film PS_{49}-*b*-$PHEMA_{51}^{224}$ when treated with polar solvents. In Figure 6A the color change after 30 min in different polar solvents is shown. Methanol and acetonitrile turned out as selective solvents for the PHEMA domain due to the strongest color change. The complete color change of the film was observed within 10 min. To provide a sense of the responsiveness and reversibility of this effect, the progress of the appearance of the film during swelling within the initial 5 min is displayed in Figure 6B. As the methanol only penetrates through the PHEMA matrix, the PS matrix is not affected, and the main structural features remain. Therefore, the color change predominantly refers to the amount of solvent penetrating the system, which gradually lowers the refractive index of the PHEMA matrix and is restricted by the initial spacing of the

© 2025 The Author(s). Advanced Materials Interfaces published by Wiley-VCH GmbH

21967350, 2026, 1, Downloaded from https://advanced.onlinelibrary.wiley.com/doi/10.1002/admi.202500593 by Saarlandische Universitäts- Und Landesbibliothek Sulb, Wiley Online Library on [03/02/2026]. See the Terms and Conditions (https://onlinelibrary.wiley.com/terms-and-conditions) on Wiley Online Library for rules of use; OA articles are governed by the applicable Creative Commons License

21967350, 2026, 1, Downloaded from https://advanced.onlinelibrary.wiley.com/doi/10.1002/admi.202500593 by Saarlandische Universitäts- Und Landesbibliothek Sulb, Wiley Online Library on [03/02/2026]. See the Terms and Conditions (https://onlinelibrary.wiley.com/terms-and-conditions) on Wiley Online Library for rules of use; OA articles are governed by the applicable Creative Commons License

PHEMA domain. Thus, a greater refractive index difference can be obtained as methanol has a lower refractive index of 1.32 than PHEMA ($n_{PHEMA} = 1.44$). As there are only small changes in the packing of the PHEMA chains, the original color can almost be recovered by evaporation of the solvent. A small change in color was only visible for the first cycle (see Figure 6B III); subsequent cycles show faster responsiveness and full recovery of the color. To support the assumption of remaining structural features, the cross-section of PS_{49}-*b*-$PHEMA_{51}$[224] film was investigated by AFM tapping mode (see Figure 6C) in the original state (I), at the first stable state after 1 h solvent treatment (3 h drying, II) and after drying overnight at room temperature (III). The high-resolution image of the cross-section, shows the microstructure, where the biphasic polymer system is clearly visible and exhibits a comparable appearance to the TEM images. After introducing methanol for 1 h, where the PHEMA was infiltrated by methanol, an increase in height difference between both polymer domains is detectable. Since the PHEMA block segments are still connected with the nonswellable PS part, they increase only to the maximum of chain stretching. After 3 h of drying, during which the color of the BCP film had almost recovered, the first analysis of the area could be conducted. Still, slight movement of the sample due to methanol evaporation could be recognized, visualized by the tilted structure in image. The final dried structure does not differ much in height profile in comparison to surface analysis of the dry state after 3 h. Only differences in the phase signal are observable, which led to the assumption that methanol is still captured in the PHEMA domain (Figure S19, Supporting Information). All in all, the structural features remain the same; only the PHEMA phase is slightly altered, particularly at the edges of the film, which could be observed in the images of the analyzed cross-section of the BCP film (Figure 6C). In addition to the freestanding BCP films presented in this work, micellar solutions and casted films of the BCPs show photonic properties, which are covered in Figure S20 (Supporting Information).

Besides the photonic properties, the PS-*b*-PHEMA films could also be used as a drug delivery system, as PHEMA is a widely spread polymer in biomedical applications like contact lenses and hydrogels, showing great optical and anti-biofouling properties.[99–101] Thus, due to the co-continuous film structure and its solvent selectivity, the BCP film could easily be used as a retardant drug release system, where very low drug release could be realized.[102] The active substance could directly be introduced into the melting process or by loading the carrier polymer film after processing with a methanol or acetonitrile solution. This loading process was shown by introducing rhodamine B into the film (Figure S11, Supporting Information). A recently emerging and promising area of application is the administration of drugs via microneedles, where PHEMA and the use of BCPs have already been described.[103–107]

3. Conclusion

In this work, we demonstrated the synthesis of high molecular weight PS-*b*-PHEMA BCPs (>100 kg mol^{-1}) with PHEMA volume ratios up to 62 vol%. The BCPs were processed by a solvent-free hot pressing method to form freestanding, microstructured polymer films within less than 15 min. Optimization of the process parameters regarding microstructure formation was carried out and directly compared to solvent-based processes. BCPs with molecular weights higher than 140 kg mol^{-1} and PHEMA ratios ranging from 20 to 51 vol% led to unique photonic polymer films with tunable transmittance, which could be used as UV and blue light filters. Furthermore, BCP films with PHEMA ratios of 40–51 vol% exhibiting co-continuous microstructures showed reversible solvent-selective color changes, which are promising for sensor applications. Although no equilibrium morphology was obtained, structure-dependent photonic properties were observable by transmittance, reflection, and fluorescence spectroscopy. These unique properties, in combination with simplified image analysis of the TEM measurements and the impression of a regularity in microstructure observed by Z-stack investigations performed with confocal fluorescence microscopy, led to the assumption that the microstructure of the freestanding polymer films possess a disordered hyperuniform structure, able to form photonic bandgaps with low refractive index differences.

Although the hot pressing method is widely applied in material science, investigations of BCP self-assembly utilizing this approach is rarely found. Further optimization through more complex polymer microstructures or the use of additives in the hot pressing process paves the way for real-world applications by tailoring the mechanical properties to the material requirements of various areas of application. With growing industrial interest in BCPs, the demand for sustainable processes is increasing.[82,86,108–110] Among these novel renewable methods are the solvent-free and short-term processes presented in this work.

4. Experimental Section

Reagents: All chemicals were purchased from Alfa Aesar (Haverhill, MA), Sigma-Aldrich (St. Louis, MO), Fisher Scientific (Hampton, NH), ABCR (Karlsruhe, Germany), and TCI (Eschborn, Germany) and used as received unless otherwise stated. Prior to use in the anionic polymerization, THF was treated with 1,1-diphenylethylene (DPE) and *n*-butyllithium (*n*-BuLi) followed by cryo-transfer. Styrene (S) and2-(trimethylsilyloxy)ethyl methacrylate (HEMA-TMS) were dried by stirring overnight over calcium hydride (CaH_2) followed by cryo-transfer to concentrated trioctylaluminium (25 wt% solution in hexane). After final transfer, reagents were stored in a glovebox at −18 °C. Lithium chloride (LiCl) was suspended in freshly distilled THF and treated with *sec*-butyl lithium (*s*-BuLi). After removing THF under reduced pressure LiCl was dried by heating and then stored in a glovebox. Anionic polymerizations were carried out under a nitrogen atmosphere in a glovebox equipped with a Coldwell apparatus.

Characterization: *Nuclear Magnetic Resonance (NMR) Spectroscopy*: NMR spectra were recorded on a Bruker DRX 300 spectrometer (Billerica, MA) working at 300 MHz. NMR chemical shifts are referenced relative to the used solvent pyridine d5 to 8.740 ppm.[111]

Size-Exclusion Chromatography: Standard SEC was performed with a system composed of a 1260 IsoPump-G1310B (Agilent Technologies, Santa Clara, CA), a 1260 VW-detector G1314F at 254 nm (Agilent Technologies) and a 1260 RI-detector G1362A at 30 or 50 °C (Agilent Technologies), with THF or DMF/LiCl (1 mg mL^{-1}) as mobile phase (flow rate 1 mL min^{-1}) on a SDV column set (SDV 10^3, SDV 10^5, SDV 10^6) or GRAM column set (GRAM 30, GRAM 1000, GRAM 1000) from PSS (Polymer Standard Service, Mainz, Germany). Calibration was carried out using PS and PMMA standards (from PSS). For data acquisition and evaluation of the measurements, PSS WinGPC UniChrom 8.2 was used.

Differential Scanning Calorimetry (DSC): DSC measurements were performed with a Mettler Toledo DSC-1 (Columbus, OH) in a temperature range of 50–180 °C with a heating rate of 20 K min^{-1} in a nitrogen

© 2025 The Author(s). Advanced Materials Interfaces published by Wiley-VCH GmbH

atmosphere. The second heat run was used to determine the thermal properties of the polymers by using Mettler Toledo STARe14 software.

Transmission Electron Microscopy: TEM experiments were carried out on a Zeiss EM 10 or EM 10 CR (Oberkochen, Germany) at 60 kV. The shown images were recorded with a slow-scan CCD camera (Tröndle TRS; Moorenweis, Germany) or a MegaView II (Olympus; Shinjuku, Japan) in bright field mode.

Scanning Electron Microscopy: SEM measurements were performed on a high-resolution SEM XL30 FEG (Philips; Amsterdam, Netherlands) at an operation voltage of 10 kV using a secondary electron detector. Prior to SEM imaging, the samples were coated with Au or Pt/Pd using a Quorum Q300T D sputter coater.

Small-Angle X-Ray Scattering: SAXS measurements were performed using a laboratory setup (Xeuss 2, Xenocs SA, Grenoble, France). The K_α line of a copper X-ray tube with a wavelength of $\lambda = 1.54$ Å was focused on the sample with a spot size of 0.25 mm^2. 2D scattering images were recorded on a Pilatus 3R 1 M detector, located at a sample-detector distance of ≈2.5 m, calibrated using a silver behenate standard. Since all samples scattered isotropically, the data were azimuthally averaged to obtain the scattered intensity in dependence on the magnitude of the scattering vector, given by $q = (4\pi/\lambda)\sin\theta$, with 2θ denoting the scattering angle. All samples were placed directly into the beam, without the need of using a sample container.

Confocal Laser Scanning Microscopy (CLSM): Confocal microscopic investigations were performed with a Leica TCS SP8 (Leica Microsystems, Mannheim, Germany) using a HCX PL APO 63×/1.32 Oil objective. The BCPs films were investigated at different excitation (ex) wavelengths by using corresponding filter systems for recording the emission (em) as followed (ex/em): 405/408–448 nm, 552 nm/560–610 nm, 640 nm/650–700 nm. The BCP film with Rhodamine B was excited at 552 nm and detected between 560 and 610 nm. Z-stacks were recorded with a pixel size (XZ) of 40 × 40 nm. These oversampling settings were used to enable a subsequent mild Gaussian smoothing in the Z direction without reducing the Z resolution of the final images.

Atomic Force Microscopy: A Bruker Dimension Icon AFM (Bruker, Germany) was used to evaluate the change in the topography of the cross section of a BCP film produced by hot pressing. A mirror-like surface of the cross section was obtained by smoothing the cutting edge using ultramicrotomy using a Leica Ultracut UCT ultramicrotome. The film was glued with minimal contact points on a plastic petri dish. After drying overnight, the initial surface was measured. Subsequently, it was treated for 1 h with methanol, followed by 3 h drying, before the first measurement was possible due to the evaporating methanol. A final measurement of the dry state was done on the next day. All measurements were conducted at ambient conditions using Silicone cantilevers in tapping mode (model HQ:NSC19 Al BS from MikroMasch) with a typical resonance frequency of 65 kHz and spring constant of 0.5 N m^{-1}. Difference in height was extracted by the onboard NanoScope 9.40 software.

UV–vis Spectroscopy: Transmission and reflection spectra in the 200–800 nm range were recorded with an Agilent Cary 5000 UV/vis–NIR spectrometer (Agilent, United States) equipped with a Universal Measurement accessory (UMA) unit. Background correction was performed by measuring 100% light intensity and 0% transmittance by blocking the light path. The step size was 1 nm, and the accumulation time was 0.1.

Fluorescence Spectroscopy: Photoluminescence measurements were performed with a Fluorolog3 spectrofluorometer Fl3-22 (Horiba Jobin Yvon) equipped with double Czerny-Turner monochromators, a 450 W xenon lamp and a R928P photomultiplier with a photon-counting system. All emission spectra were corrected for the photomultiplier sensitivity and all excitation spectra for the intensity of the excitation source.

Dynamic Mechanical Analysis (DMA): DMA measurements were carried out using a rheometer (ARES, Waters, USA) in parallel plate geometry, diameter of 25 mm. The temperature was measured with a PT-100 sensor placed directly underneath the lower plate and in contact with it. The rheometer is equipped with a convection oven operated with nitrogen to prevent oxidation of the samples. The rheometer was preheated to 180 °C to calibrate the gap. Then, a disk of 25 mm diameter and ≈1 mm thickness of the solid sample was placed between the plates. After closing the oven, the measurement was started immediately after reaching the target temperature of 180 °C again. The measurement program to measure the complex shear modulus $G^* = G' + iG''$ consisted of 11 frequency sweeps from 20 to 0.02 Hz with 3 points per decade, with a strain amplitude of 1%. Each frequency sweep took ≈4 min.

Anionic Block Copolymerization of Styrene and 2-(Trimethylsilyloxy)ethyl Methacrylate, PS-b-P(HEMA-TMS)—Exemplary Synthesis of a PS_{76}-b-$P(HEMA\text{-}TMS)_{24}$ Featuring an Overall Molar Mass of 174 kg mol^{-1}: PS-*b*-P(HEMA-TMS) was synthesized by sequential anionic polymerization at −78 °C in THF, as reported earlier.[65–67] In brief, in an ampule equipped with a stir bar, 0.97 g styrene (9.3 mmol) were dissolved in 60 mL dry THF and cooled down to −78 °C. The polymerization was initiated by a quick addition of 3.9 µL *s*-BuLi (0.005 mmol, 1.3 M solution in hexane) and was stirred for 2 h to ensure complete conversion of styrene. A sample of the solution was taken and treated with dry methanol for SEC investigation. Afterward, 1.8 µL DPE (0.010 mmol) was added, and the solution was then stirred for a further 30 min at room temperature. After further 30 min stirring at −78 °C, 2.2 mL HEMA-TMS (10.0 mmol, stored at −18 °C) was added to the solution and the reaction was stirred overnight before termination by the addition of degassed methanol. For analytical reasons, 20 mL of the polymer solution was precipitated in a tenfold excess of water, filtered and dried under reduced pressure.

The remaining polymer solution was further processed to the PS-*b*-PHEMA by deprotection. Therefore, 2.5 mL DMF followed by a mixture of 7.2 mL conc. HCl and 26.5 mL H_2O were added to the remaining 40 mL polymer solution. After stirring for two hours the polymer was precipitated in a tenfold excess of water. The polymer was washed to neutrality and dried in vacuum. If more than 5 mol% of initial TMS groups were detectable via ^{1}H NMR spectroscopy an additional cleaning step was required (Figure S2, Supporting Information).

Hot Pressing Process of PS-b-PHEMA Powder: For the formation of free-standing PS-*b*-PHEMA films, 200 mg of polymer powder was covered with two PET foils and placed between two metal plates, which were inserted into a Collin laboratory press P200 P/M (Dr. Collin GmbH, Ebersberg, Germany). The powder was preheated to the target temperature with a pressure of 3 bar for 1 min, followed by the targeted parameters to be investigated.

Supporting Information

Supporting Information is available from the Wiley Online Library or from the author.

Acknowledgements

This research was supported by the DFG project GA2169/7-1 in association with the DFG-funded consortium for advanced paper research (DFG-PAK 962/1). The authors thank Stefan Heissler for technical support. M.P. thanks Dr. Duyu Chen and Prof. Carsten Rockstuhl for the fruitful conversations.

Open access funding enabled and organized by Projekt DEAL.

Conflict of Interest

The authors declare no conflict of interest.

Data Availability Statement

The data that support the findings of this study are available from the corresponding author upon reasonable request.

Keywords

amphiphilic block copolymers, hot-pressing, microstructures, photonic materials, self-assembly, stimuli-responsiveness

© 2025 The Author(s). Advanced Materials Interfaces published by Wiley-VCH GmbH

21967350, 2026, 1, Downloaded from https://advanced.onlinelibrary.wiley.com/doi/10.1002/admi.202500593 by Saarländische Universitäts- Und Landesbibliothek Sulb, Wiley Online Library on [03/02/2026]. See the Terms and Conditions (https://onlinelibrary.wiley.com/terms-and-conditions) on Wiley Online Library for rules of use; OA articles are governed by the applicable Creative Commons License

Received: June 27, 2025
Revised: September 5, 2025
Published online: October 6, 2025

[1] C. Cummins, R. Lundy, J. J. Walsh, V. Ponsinet, G. Fleury, M. A. Morris, *Nano Today* **2020**, *35*, 100936.
[2] G. G. Yang, H. J. Choi, K. H. Han, J. H. Kim, C. W. Lee, E. I. Jung, H. M. Jin, S. O. Kim, *ACS Appl. Mater. Interfaces* **2022**, *14*, 12011.
[3] J. G. Werner, Y. Li, U. Wiesner, *Small Sci.* **2023**, *3*, 2300074.
[4] Z. Wang, C. L. C. Chan, T. H. Zhao, R. M. Parker, S. Vignolini, *Adv. Opt. Mater.* **2021**, *9*, 2100519.
[5] A. Alvarez-Fernandez, C. Cummins, M. Saba, U. Steiner, G. Fleury, V. Ponsinet, S. Guldin, *Adv. Opt. Mater.* **2021**, *9*, 2100175.
[6] L. Guo, Y. Wang, M. Steinhart, *Chem. Soc. Rev.* **2021**, *50*, 6333.
[7] A. S. Embaye, L. Martínez-Izquierdo, M. Malankowska, C. Téllez, J. Coronas, *Energy Fuels* **2021**, *35*, 17085.
[8] S. Chu, Y. Cui, N. Liu, *Nat. Mater.* **2017**, *16*, 16.
[9] K. H. Kim, Y. Huh, I. Song, D. Y. Ryu, J. G. Son, J. Bang, *J. Polym. Sci.* **2024**, *62*, 679.
[10] C. Sinturel, F. S. Bates, M. A. Hillmyer, *ACS Macro Lett.* **2015**, *4*, 1044.
[11] M. W. Matsen, F. S. Bates, *J. Chem. Phys.* **1997**, *106*, 2436.
[12] F. S. Bates, G. H. Fredrickson, *Annu. Rev. Phys. Chem.* **1990**, *41*, 525.
[13] F. S. Bates, *Science* **1991**, *251*, 898.
[14] M. W. Matsen, T. M. Beardsley, J. D. Willis, *Phys. Rev. Lett.* **2023**, *130*, 248101.
[15] J. Lequieu, T. Quah, K. T. Delaney, G. H. Fredrickson, *ACS Macro Lett.* **2020**, *9*, 1074.
[16] H. Park, S. Jo, B. Kang, K. Hur, S. S. Oh, D. Y. Ryu, S. Lee, *Nanophotonics* **2022**, *11*, 2583.
[17] K.-C. Yang, P. Puneet, P.-T. Chiu, R.-M. Ho, *Acc. Chem. Res.* **2022**, *55*, 2033.
[18] K. Hur, Y. Francescato, V. Giannini, S. A. Maier, R. G. Hennig, U. Wiesner, *Angew. Chem., Int. Ed.* **2011**, *50*, 11985.
[19] L. Xiang, Q. Li, C. Li, Q. Yang, F. Xu, Y. Mai, *Adv. Mater.* **2023**, *35*, 2207684.
[20] S. Li, H. Lin, F. Meng, D. Moss, X. Huang, B. Jia, *Sci. Rep.* **2018**, *8*, 14283.
[21] H. Yao, Y.-P. Hsieh, J. Kong, M. Hofmann, *Nat. Mater.* **2020**, *19*, 745.
[22] R. K. Cersonsky, J. Antonaglia, B. D. Dice, S. C. Glotzer, *Nat. Commun.* **2021**, *12*, 2543.
[23] E. O. Pyzer-Knapp, J. W. Pitera, P. W. Staar, S. Takeda, T. Laino, D. P. Sanders, J. Sexton, J. R. Smith, A. Curioni, *npj Comput. Mater.* **2022**, *8*, 84.
[24] S. Liu, Y. Yang, L. Zhang, J. Xu, J. Zhu, *J. Mater. Chem. C* **2020**, *8*, 16633.
[25] A. L. Liberman-Martin, C. K. Chu, R. H. Grubbs, *Macromol. Rapid Commun.* **2017**, *38*, 1700058.
[26] M. Stefik, S. Guldin, S. Vignolini, U. Wiesner, U. Steiner, *Chem. Soc. Rev.* **2015**, *44*, 5076.
[27] Z. Wang, C. L. C. Chan, R. M. Parker, S. Vignolini, *Angew. Chem., Int. Ed.* **2022**, *61*, 202117275.
[28] H. Dau, G. R. Jones, E. Tsogtgerel, D. Nguyen, A. Keyes, Y.-S. Liu, H. Rauf, E. Ordonez, V. Puchelle, H. B. Alhan, C. Zhao, E. Harth, *Chem. Rev.* **2022**, *122*, 14471.
[29] D. Chen, M. A. Klatt, G. H. Fredrickson, *arXiv preprint arXiv:2312.08541*, **2023**, *57*, 9911.
[30] B.-H. Wu, L.-W. Zhu, Y. Ou, W. Tang, L.-S. Wan, Z.-K. Xu, *J. Phys. Chem. C* **2015**, *119*, 1971.
[31] C. Zhu, L. Tian, W. Cheng, Z. Gu, *BMEMat* **2023**, *2*, 12056.
[32] M. Appold, E. Grune, H. Frey, M. Gallei, *ACS Appl. Mater. Interfaces* **2018**, *10*, 18202.
[33] Z. Cai, Z. Li, S. Ravaine, M. He, Y. Song, Y. Yin, H. Zheng, J. Teng, A. O. Zhang, *Chem. Soc. Rev.* **2021**, *50*, 5898.
[34] T. Winter, M. Bitsch, F. Müller, S. Voskian, T. A. Hatton, K. Jacobs, V. Presser, M. Gallei, *ACS Appl. Polym. Mater.* **2021**, *3*, 4651.
[35] L. Siegwardt, M. Gallei, *Adv. Funct. Mater.* **2023**, *33*, 2213099.
[36] G. Shang, M. Eich, A. Petrov, *APL Photonics* **2020**, *5*, 060901.
[37] K. Hur, R. G. Hennig, U. Wiesner, *J. Phys. Chem. C* **2017**, *121*, 22347.
[38] S. Jo, H. Park, T. Jun, K. Kim, H. Jung, S. Park, B. Lee, S. Lee, D. Y. Ryu, *Appl. Mater. Today* **2021**, *23*, 101006.
[39] C. K. Wong, X. Qiang, A. H. Müller, A. H. Gröschel, *Prog. Polym. Sci.* **2020**, *102*, 101211.
[40] C.-Y. Chang, Y.-H. Chen, R.-M. Ho, *Phys. Rev. Mater.* **2024**, *8*, 030301.
[41] S. K. Siddique, H. Sadek, T.-L. Lee, G.-M. Manesi, A. Avgeropoulos, C.-W. Wang, C.-C. Lee, E. L. Thomas, R.-M. Ho, *Giant* **2024**, *17*, 100205.
[42] M. Florescu, S. Torquato, P. J. Steinhardt, *Phys. Rev. B: Condens. Matter* **2009**, *80*, 155112.
[43] G. Gkantzounis, T. Amoah, M. Florescu, *Phys. Rev. B: Condens. Matter* **2017**, *95*, 094120.
[44] S. R. Sellers, W. Man, S. Sahba, M. Florescu, *Nat. Commun.* **2017**, *8*, 14439.
[45] W. Shi, D. Keeney, D. Chen, Y. Jiao, S. Torquato, *Phys. Rev. E* **2023**, *108*, 045306.
[46] A. Jain, J. A. Bollinger, T. M. Truskett, *AIChE J.* **2014**, *60*, 2732.
[47] C. De Rosa, F. Auriemma, C. Diletto, R. Di Girolamo, A. Malafronte, P. Morvillo, G. Zito, G. Rusciano, G. Pesce, A. Sasso, *Phys. Chem. Chem. Phys.* **2015**, *17*, 8061.
[48] C. Huang, Y. Zhu, X. Man, *Phys. Rep.* **2021**, *932*, 1.
[49] L. J. Fetters, D. J. Lohse, S. T. Milner, W. W. Graessley, *Macromolecules* **1999**, *32*, 6847.
[50] J. D. Ferry, *Viscoelastic Properties of Polymers*, Wiley, New York **1980**.
[51] M. Doi, S. F. Edwards, *The Theory of Polymer Dynamics*, Oxford University Press, Oxford **1988**.
[52] A. Semenov, *Zh. Eksp. Teor. Fiz* **1985**, *88*, 1242.
[53] B. M. Yavitt, Y. Gai, D.-P. Song, H. H. Winter, J. J. Watkins, *Macromolecules* **2017**, *50*, 396.
[54] B. R. Sveinbjörnsson, R. A. Weitekamp, G. M. Miyake, Y. Xia, H. A. Atwater, R. H. Grubbs, *Proc. Natl. Acad. Sci. USA* **2012**, *109*, 14332.
[55] A. L. Liberman-Martin, A. B. Chang, C. K. Chu, R. H. Siddique, B. Lee, R. H. Grubbs, *ACS Macro Lett.* **2021**, *10*, 1480.
[56] L. Liberman, M. L. Coughlin, S. Weigand, F. S. Bates, T. P. Lodge, *Macromolecules* **2022**, *55*, 2821.
[57] S. E. Blosch, S. J. Scannelli, M. Alaboalirat, J. B. Matson, *Macromolecules* **2022**, *55*, 4200.
[58] S. Cui, B. Zhang, L. Shen, F. S. Bates, T. P. Lodge, *J. Am. Chem. Soc.* **2022**, *144*, 21719.
[59] M. Vatankhah-Varnosfaderani, A. N. Keith, Y. Cong, H. Liang, M. Rosenthal, M. Sztucki, C. Clair, S. Magonov, D. A. Ivanov, A. V. Dobrynin, *Science* **2018**, *359*, 1509.
[60] A. Sivokhin, D. Orekhov, O. Kazantsev, K. Otopkova, O. Sivokhina, Y. Chesnokov, M. Smirnov, A. Ovchinnikov, I. Makhov, *Polym. Chem.* **2023**, *14*, 3186.
[61] M. Plank, F. Hartmann, B. Kuttich, T. Kraus, M. Gallei, *Eur. Polym. J.* **2020**, *141*, 110059.
[62] T. Ruhl, G. P. Hellmann, *Macromol. Chem. Phys.* **2001**, *202*, 3502.
[63] C. G. Schäfer, M. Gallei, G. P. Hellmann, M. Biesalski, M. Rehahn, *Proc. SPIE* **2013**, *8816*, 116.
[64] C. G. Schäfer, B. Viel, G. P. Hellmann, M. Rehahn, M. Gallei, *ACS Appl. Mater. Interfaces* **2013**, *5*, 10623.
[65] A. Hirao, H. Kato, K. Yamaguchi, S. Nakahama, *Macromolecules* **1986**, *19*, 1294.
[66] H. Mori, O. Wakisaka, A. Hirao, S. Nakahama, *Macromol. Chem. Phys.* **1994**, *195*, 3213.

© 2025 The Author(s). Advanced Materials Interfaces published by Wiley-VCH GmbH

21967350, 2026, 1, Downloaded from https://advanced.onlinelibrary.wiley.com/doi/10.1002/admi.202500593 by Saarlandische Universitäts- Und Landesbibliothek Sulb, Wiley Online Library on [03/02/2026]. See the Terms and Conditions (https://onlinelibrary.wiley.com/terms-and-conditions) on Wiley Online Library for rules of use; OA articles are governed by the applicable Creative Commons License

[67] S. Schöttner, H.-J. Schaffrath, M. P. Gallei, *Macromolecules* **2016**, *49*, 7286.
[68] M. Szwarc, *Living Polymers and Mechanisms of Anionic Polymerization*, Springer-Verlag, Berlin **2005**.
[69] X.-F. Yang, S.-J. Ye, Q. Bai, X.-Q. Wang, *J. Fluoresc.* **2007**, *17*, 81.
[70] J. Farràs, C. Serra, J. Vilarrasa, *Tetrahedron Lett.* **1998**, *39*, 327.
[71] L. P. Voegtli, C. F. Zukoski IV, *J. Colloid Interface Sci.* **1991**, *141*, 92.
[72] C. Yoshikawa, A. Goto, Y. Tsujii, T. Fukuda, T. Kimura, K. Yamamoto, A. Kishida, *Macromolecules* **2006**, *39*, 2284.
[73] J. Cheng, R. A. Lawson, W.-M. Yeh, N. D. Jarnagin, L. M. Tolbert, C. L. Henderson, *Proc. SPIE* **2013**, *8680*, 86801.
[74] Y. Zhao, E. Sivaniah, T. Hashimoto, *Macromolecules* **2008**, *41*, 9948.
[75] M. Plank, F. V. Frieß, C. V. Bitsch, J. Pieschel, J. Reitenbach, M. Gallei, *Macromolecules* **2023**, *56*, 1674.
[76] W. Zha, C. D. Han, D. H. Lee, S. H. Han, J. K. Kim, J. H. Kang, C. Park, *Macromolecules* **2007**, *40*, 2109.
[77] D. I. Perera, R. A. Shanks, *Polym. Int.* **1995**, *36*, 303.
[78] T. Caykara, C. Özyürek, Ö. Kantoğlu, *J. Appl. Polym. Sci.* **2007**, *103*, 1602.
[79] I. W. Hamley, V. Castelletto, *Progr. Polym. Sci.* **2004**, *29*, 909.
[80] A. Semenov, *Macromolecules* **1989**, *22*, 2849.
[81] M. W. Matsen, F. S. Bates, *Macromolecules* **1996**, *29*, 7641.
[82] J. Oh, M. Shin, I. S. Kim, H. S. Suh, Y. Kim, J. K. Kim, J. Bang, B. Yeom, J. G. Son, *ACS Nano* **2021**, *15*, 8549.
[83] J. Cho, J. Oh, J. Bang, J. H. Koh, H. Y. Jeong, S. Chung, J. G. Son, *Nat. Commun.* **2023**, *14*, 8412.
[84] W. H. Nam, J. Hur, J. Cho, D. Y. Ryu, H. Ahn, J. G. Son, *Small* **2025**, *21*, 2405717.
[85] M. Pinna, J. Diaz, C. Denison, A. Zvelindovsky, I. Pagonabarraga, *Soft Matter* **2025**, *21*, 476.
[86] S. E. Lee, S. Kim, J. H. Park, H. J. Jin, H. S. Kim, J. H. Kim, H. M. Jin, B. H. Kim, *J. Polym. Sci.* **2023**, *61*, 2758.
[87] Q. Zhao, C. E. Finlayson, D. R. Snoswell, A. Haines, C. Schäfer, P. Spahn, G. P. Hellmann, A. V. Petukhov, L. Herrmann, P. Burdet, *Nat. Commun.* **2016**, *7*, 11661.
[88] M. Karaman, S. E. Kooi, K. K. Gleason, *Chem. Mater.* **2008**, *20*, 2262.
[89] S. Torquato, *J. Phys.: Condens. Matter* **2016**, *28*, 414012.
[90] M. Rothammer, C. Zollfrank, K. Busch, G. von Freymann, *Adv. Opt. Mater.* **2021**, *9*, 2100787.
[91] X. Ma, J. Q. Lu, R. S. Brock, K. M. Jacobs, P. Yang, X.-H. Hu, *Phys. Med. Biol.* **2003**, *48*, 4165.
[92] H. M. Silalahi, H.-F. Lo, J.-H. Liu, C.-Y. Huang, *Opt. Express* **2025**, *33*, 31107.
[93] L. González-Urbina, K. Baert, B. Kolaric, J. Pérez-Moreno, K. Clays, *Chem. Rev.* **2012**, *112*, 2268.
[94] Y. Tang, B. Z. Tang, *Aggregation-Induced Emission*, Springer, Berlin **2022**.
[95] R. R. Darthy, C. Venkateswaran, V. Subramanian, Z. Ouyang, N. Yogesh, *Sci. Rep.* **2023**, *13*, 17077.
[96] Q. Cheng, J. Chen, W. Cai, X. Yu, C. Wan, Y. Wang, B. Xiong, C. Huang, Z. Yang, *ACS Appl. Mater. Interfaces* **2024**, *16*, 48448.
[97] G. Jacucci, S. Vignolini, L. Schertel, *Proc. Natl. Acad. Sci. USA* **2020**, *117*, 23345.
[98] J. E. Saunders, C. Sanders, H. Chen, H.-P. Loock, *Appl. Opt.* **2016**, *55*, 947.
[99] L. Shen, J. Xie, J. Tao, J. Zhu, *J. Mater. Chem. B* **2015**, *3*, 1157.
[100] P. Maji, K. Naskar, *J. Appl. Polym. Sci.* **2022**, *139*, 52942.
[101] P. Toews, J. Bates, *Sci. Rep.* **2023**, *13*, 16685.
[102] T. Huang, P. Manchanda, L. Zhang, O. Shekhah, N. M. Khashab, M. Eddaoudi, K.-V. Peinemann, *J. Membr. Sci.* **2019**, *584*, 1.
[103] A. Prabhu, V. Baliga, R. Shenoy, A. D. Dessai, U. Y. Nayak, *Drug Delivery Transl. Res.* **2025**, *15*, 436.
[104] J.-J. Huang, T.-F. Cheng, J.-Y. Wang, *J. Polym. Res.* **2024**, *31*, 350.
[105] S. Moradi, F. Nargesi Azam, H. Abdollahi, N. Rajabifar, A. Rostami, P. Guzman, P. Zarrintaj, S. M. Davachi, *ACS Appl. Bio Mater.* **2025**, *8*, 1835.
[106] M. B. Sharma, Ö. Kap, H. A. Abdelmohsen, M. D. Ashton, G. R. Harper, M. Firlak, J. E. Aaltonen, K. A. Bolland, R. Bragg, S. P Deeley, *Global Challenges* **2023**, *7*, 2300002.
[107] S. M. Kshirsagar, T. Kipping, A. K. Banga, *Pharm. Res.* **2022**, *39*, 3301.
[108] S. R. Nowak, K. G. Yager, *Adv. Mater. Interfaces* **2020**, *7*, 1901679.
[109] J. D. Hill, P. C. Millett, *Sci. Rep.* **2017**, *7*, 5250.
[110] C. Nam, J. G. Son, Y. Kim, W. B. Lee, *Soft Matter* **2023**, *19*, 4297.
[111] S. Budavari, M. J. O'Neil, A. Smith, P. E. Heckelman, *The Merck Index*, Merck Rahway, NJ **1989**.

© 2025 The Author(s). Advanced Materials Interfaces published by Wiley-VCH GmbH

21967350, 2026, 1, Downloaded from https://advanced.onlinelibrary.wiley.com/doi/10.1002/admi.202500593 by Saarlandische Universitäts- Und Landesbibliothek Sulb, Wiley Online Library on [03/02/2026]. See the Terms and Conditions (https://onlinelibrary.wiley.com/terms-and-conditions) on Wiley Online Library for rules of use; OA articles are governed by the applicable Creative Commons License